Chemical Geology 365 (2014) 69–86

Contents lists available at ScienceDirect

Chemical Geology

journal homepage: www.elsevier.com/locate/chemgeo

A detailed geochemical investigation of post-nuclear detonation trinitite glass at high spatial resolution: Delineating anthropogenic vs. natural components

Jeremy J. Bellucci *, Antonio Simonetti, Elizabeth C. Koeman, Christine Wallace, Peter C. Burns

Department of Civil & Environmental Engineering & Earth Sciences, Notre Dame University, Notre Dame, IN 46556, United States

ARTICLE INFO

Article history:
Received 24 March 2013
Received in revised form 4 December 2013
Accepted 5 December 2013
Available online 16 December 2013

Editor: L. Reisberg

Keywords:
Nuclear forensics
Trinity
Trinitite
Laser ablation
Post-detonation materials

ABSTRACT

This study documents, for the first time, the combined abundances of major and trace elements at high spatial resolution for trinitite glass, which was produced during the first atomic weapon test (Trinity site; New Mexico, USA). The results indicate that the chemical composition of trinitite is largely dependent on the precursor mineral phases found in the arkosic sand at the Trinity site. The chemical compositions of trinitite were evaluated using principal component analysis, which indicates that trends may be attributed to mixing between an anthropogenic component and phases (both major and minor) within the arkosic sand. The resolvable anthropogenic component in trinitite is made up of metals including Al, Co, Cr, Cu, Fe, Ga, Mg, Mn, Nb, Pb, Ta, and Ti. Uranium in trinitite appears to have two sources: natural U-bearing phases and the tamper used in the device. The concentrations of volatile anthropogenic metals (Co, Cr, Cu, and Pb) are enriched in samples that originate from >74 m away from ground zero. This increase may be related to a temperature-controlled fractionation, and implies that the (lower temperature) peripheral zone of a blast site is the optimal area to sample volatile metals for nuclear forensic analysis.

1. Introduction

Nuclear proliferation is, arguably, the current greatest threat to modern civilization. An increasing number of countries are not participating in negotiations to cease the development of nuclear technologies or reduce the total number of available nuclear weapons. While it is unlikely that a traditional state would issue a nuclear strike, a significant nuclear threat exists from non-state actors or terrorist groups. The increase of undocumented/unaccounted for nuclear weapons and material enhances the likelihood of a rogue group acquiring and detonating a non-traditional nuclear device in an act of terrorism. Distinguishing the chemical composition (or signature) of a nuclear device, in terms of fuel type, fission products, and device components, is critical in order to determine the region of origin of that device. Identifying the provenance of nuclear materials is necessary for accurate source attribution. As such, chemical and isotopic characterizations of post-detonation materials are foremost goals in nuclear forensics.

Historic test sites offer a place to study post-detonation products and establish protocols that will yield rapid, accurate, and precise results. Test sites are ideal for establishing nuclear forensics protocols because the compositions of weapons employed are relatively well documented; therefore, these provide a means to verify any results gained from these investigations. "Trinitite," post-detonation materials from the first atomic weapon test conducted at the Trinity site, are available for public research and have been the focus of several previous studies (e.g., Schlauf et al., 1997; Parekh et al., 2006; Semkow et al., 2006; Eby et al., 2010; Fahey et al., 2010; Belloni et al., 2011; Bellucci and Simonetti, 2012; Bellucci et al., 2013a,b,c; Wallace et al., 2013). Therefore, trinitite samples provide ideal materials to establish post-detonation nuclear forensics techniques.

The Trinity test took place at 5:29:45 a.m. on July 16, 1945 at the White Sands Proving Grounds just south of Alamogordo, NM. The Trinity device, Gadget, was an implosion-type ^{239}Pu device. Prior to detonation, Gadget was elevated to a height of 30.5 m upon a steel tower. The 21 kt explosion yielded a mushroom cloud with a height of 15.2 to 21.3 km and a temperature of ~8430 K (Eby et al., 2010). This fireball engulfed the test site, steel bomb tower, bomb components, the surrounding desert sand, and upon cooling formed a glassy layer named "trinitite". The trinitite layer extended radially to 370 m away from ground zero (Storms, 1965). A two-step model has been proposed for the formation of trinitite: 1) production of molten glass both on the ground and in the mushroom cloud, and 2) subsequent to incorporation of solid material (non-molten mineral phases, metal, and droplets) raining down from the cloud on the upper surface of this solidifying glass (Belloni et al., 2011; Bellucci and Simonetti, 2012; Wallace et al., 2013). Trinitite formed extremely rapidly and did not have time for any physical or chemical equilibrium processes. As such, there are many different morphological types of trinitite (e.g., fallout beads,

* Corresponding author at: Laboratory for Isotope Geology, Swedish Museum of Natural History, SE-104 05 Stockholm, Sweden. Tel.: +1 301 395 5588.
E-mail address: jeremy.bellucci@gmail.com (J.J. Bellucci).

0009-2541/$ – see front matter © 2013 Elsevier B.V. All rights reserved.
http://dx.doi.org/10.1016/j.chemgeo.2013.12.001

dumbbell trinitite, red inclusions, black inclusions, white inclusions, and coke-bottle colored inclusions; Table 1, Eby et al., 2010). While each variety of trinitite contains unique forensic evidence, this study is focused on characterizing "green" trinitite, which is most common.

By examining "green" trinitite, the main purpose of this study is to help establish a geochemical point of reference for future studies on the remaining morphological types of trinitite. This goal will be accomplished by acquiring spatially resolved major and trace element analyses of "green" trinitite; this information will then be used to resolve the components derived from the Gadget and site materials (e.g., the blast tower) versus those from the surrounding geology (i.e., natural background). Of particular note, the major and trace element compositions of trinitite will yield useful information on the distribution and incorporation of device components within trinitite; however this information may not yield direct clues as to the nature of the fuel and radionuclides involved with the Trinity test. Hence, this study was performed in tandem with an investigation into the isotopic composition of radionuclides (e.g., Cs, Sr, Eu, Pu) within trinitite glass (Wallace et al., 2013).

1.1. Components from the blast tower and device

The core of Gadget was constructed of concentric shells, with a 2.5 cm diameter Be neutron initiator in the center, followed by a 9.2 cm diameter "super grade" Pu–Ga alloy core, a 22 cm diameter tamper constructed from natural U, and finally a 22.9 cm diameter boron-plastic shell (Rhodes, 1986). The core consisted of 'super-grade' Pu with a $^{240}Pu/^{239}Pu$ of .0128–0.016 (Parekh et al., 2006; Fahey et al., 2010). Surrounding the core of the device was the implosion assembly, which consisted of three concentric circles of explosives and aluminum shells (Rhodes, 1986). The explosives used in the device were of RDX, TNT, and Baratol, which is a mixture of TNT and $Ba(NO_3)_2$ (Rhodes, 1986). Several studies have documented components in trinitite likely originating from Gadget, including Cu from the wiring used in the device or monitoring equipment (Eby et al., 2010; Bellucci and Simonetti, 2012), Pb with ambiguous origins (Eby et al., 2010; Fahey et al., 2010; Bellucci and Simonetti, 2012; Bellucci et al., 2013c), and W–Ta–Ga alloy, most probably a piece of the tamper or electronics (Bellucci and Simonetti, 2012). Iron and Fe–Ti inclusions have also been observed in trinitite and have been interpreted to derive from the blast tower (Eby et al., 2010; Fahey et al., 2010; Bellucci and Simonetti, 2012).

Table 1
Samples, inclusion information, and morphological descriptions.

Sample #	Notes
1	Samples with glass-like fused top surface. This is the most common type of surface feature seen on the trinitite specimens.
2	Specimens with large gas pockets in the surface or around perimeter.
3	The bottom of each sample in this group exhibits the rough texture of the sandy desert surface, which remained untouched by the blast. The tops of the specimens have lumpy, convoluted, sand included, or otherwise irregular surfaces.
4A	These samples contain red inclusions. The red inclusions are due to the presence of copper. Copper is not native to the mineralogy of the blast area. Therefore, the copper is thought to have derived from the copper wiring used in the instrumentation on the project.
4B	These samples contain black inclusions. Black inclusions are thought to be remnants of blast tower.
4C	These samples contain light colored glass of light colored flow marks.
4D	These samples contain blue inclusions. Blue inclusions are small, glassy, white to very light robin's egg blue color. These inclusions are extremely rare. No explanation in literature.
4E	These samples contain white inclusions. White inclusions consist of small masses of the partially to totally fused white feldspar or quartz.
4F	These samples contain "Coke bottle green" color inclusions.
5A	Layered specimens have lighter colored trinitite glass bases, usually with darker colored surfaces.
5B	Unusual protuberances or casts on the bases of these specimens.
5D	Elongated, finger-like extrusions. Always found in small pieces. Very delicate and rare because they are fragile and easily broken.
5E	Lace-like specimens, always small, very delicate.
5F	Specimens with possible unfused, microscopic iron blebs.

1.2. Components from sand

The dominant surface geology at the White Sands Missile Range is arkosic sand with alluvial, aeolian, evaporatic, and volcanic components (Ross, 1948; Eby et al., 2010). Arkosic sand consists predominantly of quartz (SiO_2), K-feldspar ($KAlSi_3O_8$), and may contain minor amounts of carbonates ($CaCO_3$), sulfates ($BaSO_4$, $CaSO_4 \cdot 2H_2O$), chlorides (NaCl), and detrital zircon ($ZrSiO_4$); other U-bearing trace mineral phases include monazite (REE, Th, PO_4) and apatite ($Ca_5(PO_4)_3$ (F, Cl, OH)). Also present are clay and mafic minerals, specifically hornblende (Ca_2(Mg, Fe, Al)$_5$(Al, Si)$_8O_{22}(OH)_2$), olivine ($(Fe, Mg)_2SiO_4$), magnetite (Fe_3O_4), ilmenite ($FeTiO_3$), and augite ((Ca, Na) (Mg, Fe, Al, Ti) (Si, Al)$_2O_6$); (Ross, 1948; Staritzky, 1950; Pettijohn, 1963; Love et al., 2008; Eby et al., 2010; Fahey et al., 2010). Knowledge of the pre-detonation geology is of critical importance in order to resolve the addition of chemical components originating from the bomb and those from the surrounding blast site; detection and identification of these components is a foremost goal of a nuclear forensics study. Metals abundant in both the device and blast tower, such as Fe and U are typically present at low abundances in arkosic sandstone (e.g., <1 wt.% FeO_{Total}; Pettijohn, 1963). Additionally, Pu and related activation/fission products would have been non-existent in a natural environment at the time of the test. Hypothetically, these elements will provide the best avenue for discerning components from the test site, Gadget, and surrounding geology (e.g., Wallace et al., 2013).

Of utmost importance, as shown here in Figs. 1 and 2 and in previous investigations (Eby et al., 2010; Fahey et al., 2010; Wallace et al., 2013), trinitite is extremely heterogeneous (petrographically and chemically) at the micron scale. Therefore, a variety of micro-analytical techniques are necessary to effectively evaluate the compositional and isotopic distributions in trinitite and potentially resolve any device components/mixing end-members (e.g., Hainley et al., 2012; Koeman et al., 2012). For example, the recent study by Wallace et al. (2013) reports combined alpha and beta radiography results (maps) in conjunction with scanning electron microscopy (SEM)–back scatter electron (BSE) imaging; the former indicate areas within trinitite that are abundant in alpha (U, Pu) and beta emitter (Cs) radionuclides. Hence, this combined, multiple imaging and LA–(MC)–ICP-MS analysis methodology results in an efficient manner for documenting isotopic variations of radionuclides at high spatial resolution (10s of micron scale; Bellucci et al., 2013b,c; Wallace et al., 2013).

The major element chemical maps indicate that trinitite is composed of relict quartz and feldspar grains and a heterogeneous melt glass (Figs. 1, 2), and supports the earlier observations by Eby et al. (2010). This study is explicitly focused on identifying and characterizing the composition of chemical components, other than quartz, that were incorporated into the melt glass. Subsequently, mixing end-members are determined using traditional geochemical techniques and the statistical multivariate analytical technique, principal component analysis (PCA). Electron microprobe analysis (EMPA) and laser ablation–ICP-MS techniques provide the means to quantitatively determine the abundances of both major (concentrations of >1 wt.%) and trace elements, respectively, in situ with spatial resolution on the scale of 10s of microns. Utilizing these techniques, the first detailed spatially resolved geochemical investigation of trinitite melt glass is reported here.

2. Samples

All of the samples of trinitite analyzed here (n = 13) were purchased from Mineralogical Research Corporation (www.minresco.com). The samples have wide range of morphologies but generally consist of trinitite melt glass on the top surface (i.e., exposed to blast) and transition into un-melted desert sand towards the bottom side

(Table 1). Prior to in situ analysis, samples were cut into polished thin sections with a thickness of 60–100 μm. The Trinity site was bulldozed in 1954 and the glassy layer of trinitite was buried (US GPO, 2000). As a result, all trinitite samples lack constraints on their exact original location within the Trinity blast site. Therefore, alternate methods can be employed in an attempt to place the trinitite samples in a spatial context (e.g., Parekh et al., 2006; Belloni et al., 2011; Bellucci et al., 2013a). Bellucci et al. (2013a) measured the activity of ^{152}Eu by gamma spectroscopy for the samples studied here, which was subsequently used to estimate the distance away from ground zero; this yielded calculated distances from ground zero between 51 and 74 m (Bellucci et al., 2013a). Additionally, several samples analyzed lacked ^{152}Eu activity, and therefore, presumably originate from a greater distance relative to ground zero. The calculated distances and their associated 1σ uncertainties for the samples investigated here are listed in Table 3.

3. Analytical methods

All analyses (n = 119) on 13 samples were conducted on trinitite glass (Figs. 1, 2) and one pristine K-feldspar crystal (width = 5 cm). Due to the high degree of heterogeneity within each sample, great caution was taken to select spots that were representative of the heterogeneous nature of the trinitite glass within each sample but homogeneous enough to analyze one melt glass "phase" per analysis. Specifically, the spots analyzed were homogeneous relative to their backscatter electron images (i.e., major element composition) in a radius of at least ~75 μm (Fig. 2). Chemical maps (Figs. 1, 2) were constructed utilizing an EDAX Orbis Micro EDXRF system with the analytical settings presented in Table 2.

Major element analyses were conducted at the University of Chicago with a Cameca SX-50 electron microprobe using the parameters listed in Table 2. Standardization was performed using well-characterized in-house standards of olivine (FeO, MgO, MnO), albite (Na_2O), anorthite (CaO, Al_2O_3), asbestos (SiO_2), microcline (K_2O), and rutile (TiO_2). Internal uncertainties ($2\sigma_{mean}$) are based on counting statistics, and are ≤2% for SiO_2, Al_2O_3, and CaO; ≤5% for FeO, Na_2O, and K_2O; and ≤10% for MnO, MgO, and TiO_2.

All in situ trace element analyses were performed within MITERAC (Midwest Isotope and Trace Element Research Analytical Center) at the University of Notre Dame. Measurements were carried out using a New Wave Research UP-213 frequency quintupled Nd:YAG laser ablation system coupled with a Thermo Finnigan Element 2 sector field ICP-MS. Analytical conditions and settings are listed in Table 2 and similar to those presented in Chen and Simonetti (2013). Background counts were determined for 60 s with the laser on and shuttered. Sample ion signal was collected for 60 s subsequent to the start of ablation. Concentrations were determined using the NIST SRM 612 glass wafer as the external standard and CaO wt.% (obtained by electron microprobe) as the internal standard. Data reduction was performed offline using *Glitter* software, which yields concentrations, internal uncertainties,

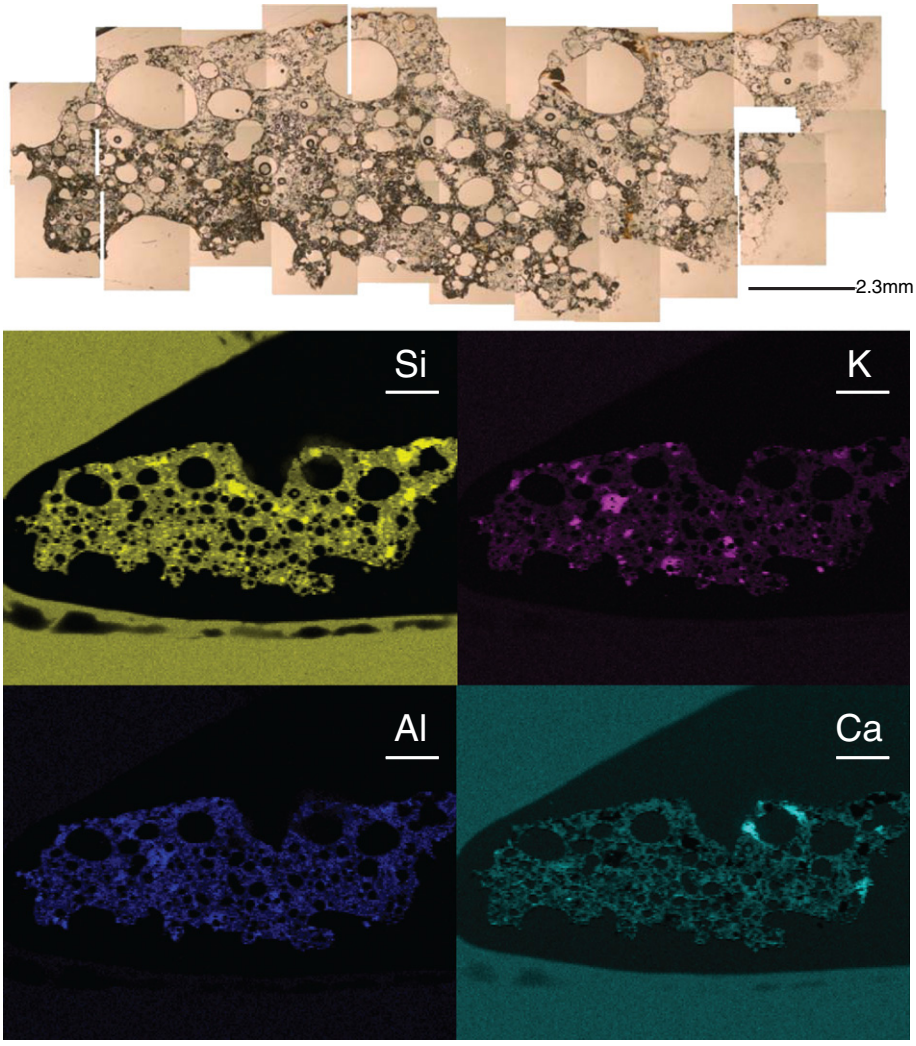

Fig. 1. A plane polarized photomicrograph of a section of trinitite with corresponding micro XRF mapping. Scale bar in all panels is 2.3 mm.

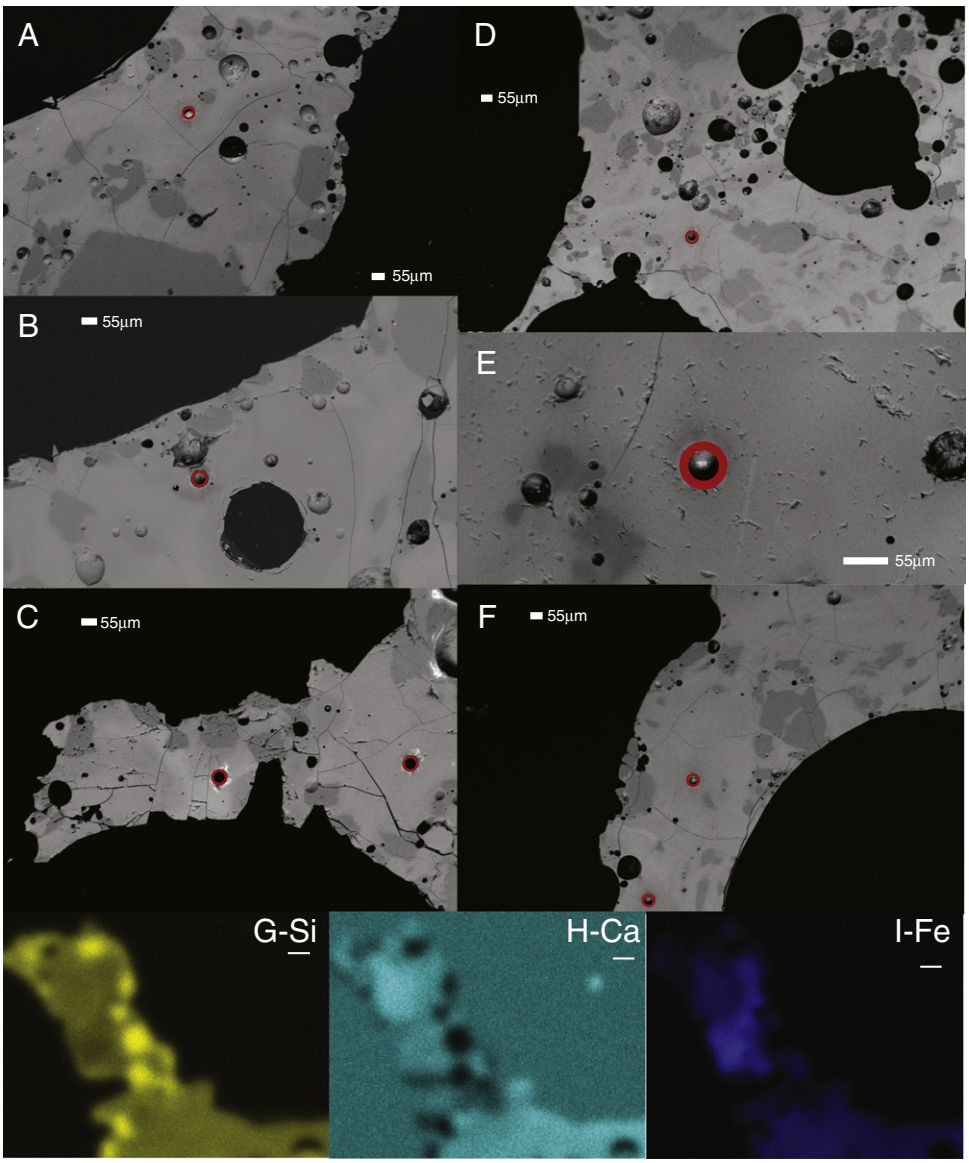

Fig. 2. Several backscatter electron images of different samples of trinitite glass with location of laser pits of 55 µm (red circles) identified. Each picture was taken at a different scale to emphasize the heterogeneity of an individual sample, and used for selecting areas for analysis. Dark areas (represent areas of lower, average atomic number) are relict quartz grains and lighter areas (areas of higher, average atomic number) are those of the trinitite melt glass characterized in this study. Additionally, micro XRF maps of Si, Ca, and Fe of BSE image C are shown in G, H, and I, respectively. Scale bar in XRF maps is 100 µm.

and levels of detection (van Achterbergh et al., 2001, http://www.glitter-gemoc.com). The average internal uncertainty ($2\sigma_{mean}$) is a function of the absolute abundance of each trace element and for most elements investigated in this study is ~10%. No significant signal changes were observed in the time resolved spectra (depth), further indicating the successful analysis of an individual, homogenous 55 µm diameter of trinitite melt glass.

The trace element composition of the desert sand was determined by collecting loose, un-melted sand from the bottom side of several ($n = 5$) trinitite samples. Three aliquots of sand, weighing between 80 and 200 mg each, were digested using a concentrated HF:HNO_3 acid mixture (4:1 ratio) in 15 ml Savillex® Teflon vials (capped) on a hotplate set at 150 °C for ~48 h in a clean room (class 1000) laboratory. Samples were then evaporated to dryness followed by the addition of 2 ml concentrated HNO_3, and the solutions were then placed on the hotplate for an additional 24 h. This procedure was repeated twice. Subsequent to the last evaporation cycle, 5 ml of concentrated HNO_3 was added and then diluted gravimetrically to a final volume of ~100 ml with 18 MΩ water. The abundances of the trace elements investigated here were determined by a standard/spike addition method (after Jenner et al., 1990), which includes corrections for matrix effects and instrumental drift. Optimization of the ICP-MS instrument was achieved with the use of a multi-element 1 ppb tuning solution. Instrument tuning consisted of optimization of torch assembly position, sample gas (Ar) flow rate, ion lens stack voltages, and reference mass calibration. All solution mode analyses were conducted using the same Thermo Finnigan Element 2 ICP-MS instrument as employed for the laser ablation analyses. Solution mode analyses were performed in medium mass resolution (resolution = mass / peak width ~ 4000) in order to eliminate any potential spectral interferences. After optimization and tuning, a 1 ppb solution of U typically yielded approximately 50,000 cps of ion signal in medium mass resolution.

Table 2
Analytical settings.

Cameca 1 electron microprobe[a]	
Accelerating voltage	15 kV
Beam size	15 μm
Beam current	35 nA
EDAX Orbis Micro EDXRF[b]	
X-ray aperture size	30 μm
Voltage	20 kV
Amperage	495 μA
Time	12.8 μs
Matrix	256 × 200 pixels
Dwell	200 μs
Spectrum map	16 bit
Acquisition time	2.5 h
Thermo Finnigan Element 2[b]	
Forward power	1250 W
Reflected power	1 W
Cool gas (Ar)	16.61 l min^{-1}
Aux gas (Ar)	0.98 l min^{-1}
Sample gas (He)	0.6 l min^{-1}
Guard electrode	Enabled
Dwell time	8 ms
Samples per peak	1
Resolution	Low
Scan type	Escan
Th/ThO	<1%
Isotopes measured	^{43}Ca[c], ^{53}Cr, ^{59}Co, ^{65}Cu, ^{71}Ga, ^{85}Rb, ^{86}Sr, ^{89}Y, ^{92}Zr, ^{93}Nb, ^{117}Sn, ^{133}Cs, ^{138}Ba, ^{139}La, ^{140}Ce, ^{141}Pr, ^{146}Nd, ^{147}Sm, ^{153}Eu, ^{160}Gd, ^{159}Tb, ^{163}Dy, ^{165}Ho, ^{166}Er, ^{169}Tm, ^{172}Yb, ^{175}Lu, ^{180}Hf, ^{181}Ta, ^{208}Pb, ^{232}Th, ^{238}U
New Wave UP-213	
Spot size (diameter)	55 μm
Fluence	10 J cm^{-2}
Repetition	7 Hz

[a] University of Chicago.
[b] University of Notre Dame.
[c] Internal standard.

4. Results

Trace element data for the un-melted sand analyzed here are listed in Table 3. With the exception of a few elements (e.g., Pb, Ta, Rb, Co, and Ga), the composition of the sand listed in Table 3 is similar to that for the upper continental crust reported by Rudnick and Gao (2003) (sand/upper continental crust ~ 1 ± 0.5). Enrichments in Pb, Ta, and Rb (sand/upper continental crust > 1.5) and depletions in Co and Ga (sand/upper continental crust < 0.5) are recorded. Of note, the enrichments in Ta and Pb measured for the un-melted sand may result from the incorporation of micro inclusions (diameter ~ 10 μm) shaken loose from the top surface of trinitite (Bellucci and Simonetti, 2012).

Compared to the 'average' major element composition of arkoses (Pettijohn, 1963), which typically range between 70 and 85 wt.% SiO_2, 7–14 wt.% Al_2O_3, <3.0 wt.% CaO, and 3–6 wt.% K_2O, the majority of the trinitite analyses reported here overlap these ranges with the notable exceptions of lower SiO_2 and higher CaO abundances (Fig. 3). The lower SiO_2 content is most likely due to the completed objective of avoiding relict quartz grains during the laser ablation analyses. As discussed by Pettijohn (1963), the relative concentrations of the major elements present within sand (or sandstones) are dependent on the modal abundances of the constituent minerals, such as K-feldspar, quartz, plagioclase, and calcite (or carbonate). Hence, the lower SiO_2 and higher CaO contents of trinitite melt glass compared to those for typical arkosic sand (Pettijohn, 1963) indicate that the latter at the Trinity site is more calcareous in nature. This result is not surprising given that there are significant gypsum deposits in the area. Fig. 4 shows a well-defined correlation between SiO_2 and CaO abundances indicating a two end-member mixing line between a SiO_2-rich major phase (quartz) and a CaO-rich major phase (calcite/gypsum). The well-defined correlation between K_2O and Rb abundances (Fig. 4) indicates the importance of the chemical signature imparted by precursor K-feldspar to trinitite melt glass. Iron oxide (FeO) contents range from 0.8 to 7.5 wt.% (Fig. 3); however, most trinitite analyses contain between 1 and 4 wt.% FeO and are within the typical range recorded in arkosic sands (Pettijohn, 1963). Of interest, the abundances of MgO and TiO_2 define the best correlations relative to FeO contents (Fig. 3), and both these elements are typically present at very low concentrations (≪1 wt.%) in arkosic sand (Pettijohn, 1963). Overall, the major element composition of trinitite is highly variable (Tables 3, 4 and Fig. 3). Each major element displays a similar standard deviation of ~30% (1σ) with MnO having the largest (53%) and SiO_2 having the smallest (9%). Despite the large degree of chemical heterogeneity, the calculated average concentrations for the major elements (Table 4) are similar to those reported by Eby et al. (2010) and Fahey et al. (2010).

As with the major elements, the concentrations of the trace elements in trinitite are highly variable (Tables 3, 4 and Figs. 4, 5). Most trace elements have a standard deviation of ~50% (1σ). Exceptions to this observation are Cu (164%), Zr (167%), Hf (176%), Pb (231%), Th (282%), and U (97%). The extreme ranges recorded for these elements can be attributed to individual, less common phases contributing to each end-member. These end-members will be discussed below. In contrast, barium displays the most consistent trace element abundance with a standard deviation of 34% (1σ). The trace element composition for 'average' arkosic sand is difficult to establish since it is primarily controlled by elemental substitutions within the constituent minerals, and the presence of accessory minerals, such as zircon, monazite, and apatite (e.g., Pettijohn, 1963). The average concentrations for most of the trace elements in trinitite reported here are similar to those of the sand present at the Trinity site (trinitite/sand ~ 1), with marked depletions (trinitite/sand < 0.5) in Zr, Sn, and enrichments (trinitite/sand > 1.5) in Sr, Eu, Gd, Tb, Pb, Th, and U. Some analyses are characterized by unique compositions (Table 4). For example, analysis 5d-1.72b-09 has extremely high concentrations of Th, La, and Ce; 1-3.59a-06 contains the highest abundances of Ti, Hf, and Zr; 4d-9.18a-05 records abundant Sr and Ca; 4c-10.6a-10 has significant Rb, Cs and Ba; and 4a-1.95a-01 is characterized by an elevated Sn content.

5. Discussion

5.1. Major elements

Bivariate diagrams of major elements vs. FeO illustrate the most apparent mixing patterns (Fig. 3). The vast majority of the trends observed for the major element abundances can be attributed to mixing between the phases present in arkosic sand: quartz, K-feldspar, and calcite/gypsum. Additionally, there are several major elements that have concentrations higher than what can be expected based on the mineralogy of the arkosic sand, and therefore these elements could be, in part, of anthropogenic origin (i.e., Al, Fe, Ti, Mn, and Mg; Fig. 3). For example, the major Al-bearing phases in arkosic sand are K-feldspar and plagioclase, which typically have Al_2O_3 contents of ~18 wt.%, depending on the type of plagioclase (Fig. 3). There are several analyses of trinitite glass that contain Al_2O_3 contents of ≥18 wt.% and therefore the latter cannot be attributed to the precursor minerals found in the arkosic sand, especially when dilution by other phases is taken into account. Thus, one possibility is that the higher Al contents derive from the aluminum shells contained within the device. Linear trends are also defined by the abundances of 'metallic' major elements (i.e., TiO_2, MnO, MgO) vs. FeO (Fig. 3). Enrichments in Fe could be attributed to mixing with trace mafic phases in the sand (e.g., amphibole, ilmenite). However, at high FeO wt.% contents the MgO/FeO, MnO/FeO, and TiO_2/FeO ratios 'fractionate' (deviate), which is indicative of non-stoichiometric behavior (i.e., non-linear trends in Fig. 3). Stoichiometric behavior is expected if mixing with predominantly mafic minerals occurs, as Fe, Mg, and Mn substitute for each other, and the TiO_2/FeO

Table 3
Major and trace element compositions of trinitite and un-melted sand.

Sample number	Distance[a]	1σ[a]	FeO	MnO	Na_2O	Al_2O_3	MgO	SiO_2	TiO_2	K_2O	CaO	Sum	Cr[b]	Co	Cu	Ga	Rb	Sr	Y	Zr	Nb
Th enriched n = 6																					
1-3.59a-10			1.6	0.076	1.7	10.3	0.9	54.9	0.36	1.8	26.0	97.6	17	4.1	13.3	7.3	39	288	22	53	6.1
4e-5.22b-03	60	7	2.7	0.059	1.9	13.0	1.0	68.0	0.49	3.0	8.8	99.0	62	8.8	9.5	14.5	137	264	62	73	15.9
4e-5.22b-09	60	7	2.2	0.056	2.3	13.4	0.8	69.8	0.42	3.5	5.6	98.0	85	6.3	5.6	8.0	101	174	14	28	9.0
4f-2.36a-03			2.6	0.061	2.3	16.3	1.1	62.8	0.46	3.7	7.3	96.5	28	6.4	22.1	8.4	187	269	20	96	13.7
5A-6.06-4	51	2	3.8	0.093	2.3	15.3	1.8	60.3	0.65	2.3	12.5	99.1	40	6.1	6.3	14.7	95	459	24	79	11.1
5d-1.72b-09	74	7	2.1	0.059	1.6	11.1	0.8	73.6	0.43	3.2	5.8	98.6	20	3.3	5.2	20.6	78	153	21	94	7.9
Nb and Ta enriched n = 6																					
4b-2.64b-04	55	6	2.5	0.045	1.3	14.4	0.8	69.0	0.45	2.6	7.3	98.4	26	8.0	4.2	3.7	107	221	13	56	16.6
4c-10.6a-03	67	5	3.1	0.010	1.6	13.1	0.8	69.9	0.38	3.6	5.3	97.7	18	3.3	9.3	3.1	92	225	14	55	41.7
4f-2.36a-10			2.0	0.036	2.5	15.1	1.3	65.1	0.46	3.6	6.0	96.0	30	4.4	74.4	10.2	115	199	14	106	14.0
4f-2.36a-11			1.7	0.046	2.3	14.4	0.7	66.3	0.40	4.1	5.8	95.7	39	5.0	34.9	8.7	112	208	13	34	33.0
5b-10.4b-07	58	5	1.6	0.010	1.8	14.4	0.6	68.6	0.33	5.5	4.8	97.6	18	3.6	7.7	10.5	233	286	9	32	11.7
5d-1.72b-04	74	7	3.0	0.057	1.9	13.6	1.2	66.8	0.53	3.4	7.8	98.3	53	5.8	9.7	10.1	95	232	15	44	16.4
Zr enriched n = 25																					
1-3.59a-04			3.2	0.070	2.2	14.2	1.6	58.9	0.57	2.8	14.4	98.0	28	6.3	30.6	12.6	106	308	26	117	13.0
1-3.59a-05			3.4	0.046	1.9	13.9	1.3	62.8	0.52	3.8	8.7	96.3	24	5.3	8.9	8.9	98	224	24	195	9.3
1-3.59a-06			4.1	0.044	1.2	13.1	1.3	63.2	1.05	1.8	10.9	96.6	27	5.0	7.5	4.2	45	284	42	1682	12.2
3-5.2a-04			2.8	0.070	1.4	14.0	1.3	66.7	0.71	2.2	8.4	97.6	28	8.5	8.9	3.3	64	237	30	153	16.1
3-5.2a-08			2.9	0.080	2.0	14.1	1.5	61.7	0.69	2.9	10.2	96.0	35	11.6	312.3	11.1	94	242	23	117	16.6
4b-2.64b-05	55	6	2.6	0.045	1.4	12.4	0.9	71.1	0.74	2.8	6.3	98.3	39	8.3	5.5	5.6	82	175	13	117	10.8
4b-2.64b-06	55	6	4.2	0.071	1.9	13.9	1.1	66.7	0.47	2.6	7.3	98.2	117	8.7	6.8	6.1	88	216	16	198	9.4
4c-10.6a-01	67	5	2.4	0.052	1.6	14.9	0.9	66.6	0.40	3.4	7.6	97.9	27	5.0	12.4	6.8	167	242	13	179	11.6
4c-10.6a-02	67	5	2.8	0.049	2.2	15.7	1.1	64.3	0.61	3.3	8.1	98.2	42	8.0	26.4	18.1	156	266	21	188	17.2
4c-10.6a-04	67	5	2.5	0.058	1.9	14.9	0.9	67.1	0.43	3.0	6.7	97.5	23	4.0	5.0	6.6	90	239	21	259	13.6
4c-10.6a-09	67	5	3.1	0.046	1.5	14.3	1.2	65.6	0.53	2.7	8.2	97.2	22	4.9	19.2	5.6	75	226	21	416	11.8
4e-5.22b-06	60	7	1.8	0.027	2.2	17.1	0.8	64.9	0.50	4.3	6.7	98.4	22	6.2	7.8	8.6	199	229	23	193	20.1
4f-2.36b-5			2.6	0.037	1.5	13.2	1.1	61.7	0.47	2.0	15.0	97.6	34	6.2	28.8	8.5	86	349	44	191	14.1
4f-2.36b-6			3.6	0.074	1.9	13.1	1.4	63.0	1.55	2.5	9.2	96.4	39	7.1	11.2	7.6	50	242	20	181	25.6
4F-5.37-01	51	4	2.8	0.035	0.9	16.6	1.3	53.0	0.46	1.0	22.0	98.2	22	3.2	5.9	2.0	64	506	37	192	11.7
4F-5.37-02	51	4	3.6	0.075	0.8	13.4	1.4	55.4	0.41	0.7	22.3	98.0	31	3.3	7.7	2.9	40	559	38	176	11.7
4F-5.37-03	51	4	2.5	0.058	0.9	15.3	1.2	57.9	0.45	1.5	19.3	99.1	20	2.1	6.4	2.0	31	538	26	179	10.2
4F-5.37-04	51	4	3.0	0.070	0.6	18.5	1.3	51.4	0.40	0.8	22.3	98.4	19	2.4	4.9	3.0	48	561	34	148	9.9
4F-5.37-09	51	4	2.7	0.021	0.9	14.7	1.2	57.7	0.46	1.4	19.2	98.1	16	2.5	6.7	2.6	44	501	23	141	10.4
4F-5.37-10	51	4	2.8	0.000	0.7	17.1	1.2	53.2	0.44	1.4	22.1	99.0	15	4.2	24.5	2.3	57	564	38	232	10.9
4F-5.37-11	51	4	2.8	0.045	0.7	15.5	1.2	53.1	0.44	1.1	23.9	98.9	33	3.1	4.5	4.7	85	623	30	163	11.2
5A-6.06-5	51	2	2.1	0.070	1.4	11.1	1.0	58.0	0.28	1.9	22.9	98.6	45	9.6	28.4	10.4	230	741	31	133	14.0
5b-10.4b-04	58	5	2.2	0.052	2.6	13.0	1.0	70.2	0.38	3.7	5.8	98.9	34	5.9	10.7	13.6	174	246	19	171	9.9
5d-1.72b-03	74	7	3.1	0.058	1.4	12.7	1.2	67.9	0.34	3.2	8.3	98.1	22	5.2	7.8	12.4	93	208	14	145	10.8
5d-1.72b-10	74	7	4.3	0.056	1.2	13.3	1.2	66.9	0.70	2.2	8.7	98.7	29	5.4	5.6	6.7	66	209	21	151	11.7
U enriched n = 44																					
1-3.59a-01			3.6	0.097	1.6	13.1	1.2	63.7	0.69	1.9	10.2	96.2	19	4.7	8.2	4.3	38	267	23	70	12.9
1-3.59a-02			3.4	0.035	1.4	12.3	1.1	66.3	0.59	2.1	9.3	96.5	87	3.6	6.7	2.7	28	219	18	52	9.2
1-3.59a-03			3.3	0.085	2.2	14.1	1.4	59.7	0.51	3.1	13.8	98.1	30	6.3	49.5	10.0	85	262	22	57	11.6
1-3.59a-07			2.8	0.045	1.1	10.1	1.3	65.8	0.86	2.3	12.4	96.7	26	5.1	4.6	4.0	51	237	16	49	16.7
3-5.2a-01			3.4	0.058	1.3	16.0	1.6	62.2	0.76	1.8	9.8	96.9	33	10.7	9.0	6.1	84	220	32	32	14.1
3-5.2a-02			3.4	0.068	1.2	13.9	1.4	63.2	0.62	2.5	10.4	96.7	61	10.7	9.0	6.4	73	251	19	78	13.7
3-5.2a-06			2.5	0.061	1.7	15.1	1.2	64.8	0.51	2.9	9.0	97.7	33	8.9	34.8	7.2	81	245	18	49	10.8
3-5.2a-10			3.1	0.066	1.5	12.8	1.8	65.5	0.68	2.4	10.0	97.7	50	13.9	42.7	9.2	77	282	23	106	13.3
4a-1.95a-02			3.3	0.081	1.1	13.7	1.6	62.4	0.98	2.1	13.5	98.8	59	11.4	17.6	6.5	98	300	20	48	16.8
4a-1.95a-03			3.0	0.054	1.1	13.9	1.3	64.1	0.70	3.2	10.6	97.9	24	16.5	12.1	4.4	69	220	17	66	9.1
4a-1.95a-04			2.9	0.050	1.1	11.4	1.9	66.9	0.33	1.7	12.2	98.5	136	10.1	16.1	4.8	71	284	15	43	12.0
4a-1.95a-06			2.3	0.048	1.0	9.4	1.1	52.0	0.39	1.8	30.1	98.0	28	15.1	35.2	6.3	51	458	11	42	8.0
4a-1.95a-07			2.3	0.076	1.2	9.7	1.0	53.3	0.40	1.9	28.9	98.7	31	14.7	35.6	6.6	63	442	16	40	7.4
4b-2.64b-02	55	6	3.2	0.057	1.2	9.1	1.1	73.4	0.39	2.2	7.7	98.3	23	8.8	19.0	3.5	68	152	23	12	10.3
4b-2.64b-03	55	6	4.9	0.065	1.3	19.5	1.4	57.4	0.53	1.7	10.9	97.6	15	8.7	6.3	1.7	32	255	15	45	10.8
4b-2.64b-10	55	6	3.2	0.065	1.3	21.9	1.2	55.9	0.52	1.7	11.9	97.7	24	10.3	5.7	2.1	50	279	26	86	12.0
4b-2.64b-9	55	6	0.7	0.009	2.6	18.4	0.2	64.9	0.11	10.4	1.3	98.6	9	1.3	11.6	12.1	292	19	5	6	0.4
4c-10.6a-08	67	5	2.4	0.066	1.1	7.5	1.1	58.8	0.40	1.7	19.5	92.6	25	4.9	17.1	6.0	54	370	17	89	8.1
4d-9.18a-03	68	7	1.2	0.032	0.7	5.3	1.1	61.3	0.26	0.7	27.9	98.5	60	17.0	22.1	4.4	22	632	29	76	7.8
4d-9.18a-07	68	7	3.2	0.074	2.2	16.0	1.4	61.6	0.67	3.2	9.4	97.8	26	9.1	34.5	6.3	80	243	20	85	11.4
4d-9.18a-09	68	7	1.9	0.014	1.9	12.0	0.8	70.6	0.43	3.1	6.9	97.6	29	7.2	10.9	4.3	57	261	23	54	10.7
4d-9.18a-10	68	7	2.4	0.067	1.6	13.9	1.1	67.2	0.65	3.6	8.8	99.2	26	8.4	10.3	6.8	84	221	19	58	11.7
4d-9.18a-11	68	7	2.8	0.034	1.4	13.4	1.3	66.1	0.58	2.7	10.7	98.8	24	9.5	7.5	7.1	68	256	20	56	11.3
4e-5.22b-07	60	7	2.2	0.076	1.9	12.5	1.0	71.0	0.41	2.7	5.4	97.3	26	6.6	7.7	7.4	99	170	46	41	10.9
4e-5.22b-10	60	7	2.3	0.025	1.8	12.1	1.0	71.9	0.44	4.2	5.6	99.4	29	6.5	6.7	6.5	127	182	18	75	10.1
4e-5.22b-11	60	7	2.2	0.081	2.2	16.5	0.9	64.7	0.36	4.3	6.9	98.0	33	7.4	8.7	9.5	97	198	30	52	12.1
4f-2.36a-02			2.3	0.022	1.7	11.9	1.0	66.4	0.45	2.9	10.1	96.8	45	6.8	32.1	13.3	91	351	24	107	14.1
4f-2.36b-1			1.6	0.000	0.8	6.8	0.9	47.5	0.31	1.2	38.4	97.6	26	3.9	19.9	5.0	35	753	11	51	4.7
4f-2.36b-2			1.9	0.027	0.9	7.5	0.9	49.6	0.30	1.7	34.6	97.5	27	3.4	16.3	4.4	31	682	10	43	4.4
4f-2.36b-3			2.2	0.032	0.9	8.0	0.9	49.3	0.37	1.6	34.6	97.9	27	4.0	11.4	5.4	41	683	12	56	5.9

Sn	Cs	Ba	La	Ce	Pr	Nd	Sm	Eu	Gd	Tb	Dy	Ho	Er	Tm	Yb	Lu	Hf	Ta	Pb	Th	U
0.8	1.1	449	19	27	4.1	17	3.6	0.8	4.0	0.6	3.9	0.8	2.2	0.3	2.2	0.3	4.2	0.6	37	85	7.0
0.8	4.3	816	131	145	30.9	124	23.7	2.7	28.7	4.0	13.9	2.3	7.9	0.8	4.9	0.7	6.3	1.0	11	448	8.6
0.8	3.1	681	18	43	4.2	15	3.1	1.1	3.3	0.5	2.6	0.5	1.7	0.3	1.8	0.2	2.5	0.5	7	57	3.5
1.3	5.0	1080	61	51	17.4	56	10.3	1.6	6.5	0.9	4.7	0.7	2.0	0.3	2.1	0.3	6.5	0.8	937	57	5.3
	3.1	754	32	48	7.2	30	6.0	1.4	5.2	0.8	4.6	0.8	2.3	0.3	2.4	0.3	3.6	0.8	12	66	4.3
1.0	2.0	550	168	362	39.0	140	24.6	1.9	15.8	1.6	5.4	0.8	2.2	0.3	2.1	0.3	5.6	0.7	5	144	4.1
1.4	3.8	466	15	33	3.5	14	2.4	1.5	4.1	0.6	2.2	0.4	1.6	0.2	1.9	0.2	5.1	2.1	2	7	3.5
0.8	2.5	776	26	54	6.3	23	4.2	0.8	3.3	0.5	2.6	0.5	1.5	0.2	1.7	0.3	3.7	3.2	1	9	6.9
1.3	3.0	682	16	33	3.9	14	2.5	0.7	2.3	0.4	2.0	0.4	1.4	0.2	1.8	0.2	5.6	1.3	681	5	2.5
1.1	3.1	724	19	43	4.6	17	3.2	0.8	2.5	0.4	2.5	0.4	1.3	0.2	1.6	0.2	2.3	3.8	813	7	2.6
1.7	8.3	123	11	31	3.2	12	2.2	0.9	1.6	0.2	1.4	0.3	0.9	0.1	1.0	0.2	1.8	1.3	25	11	1.7
1.3	3.0	512	15	42	4.5	18	3.7	1.0	3.2	0.5	2.9	0.5	1.6	0.2	1.5	0.2	2.8	1.0	17	5	5.6
2.5	3.3	835	32	53	6.8	28	5.2	1.1	4.7	0.7	4.3	0.9	2.7	0.4	3.0	0.5	8.7	1.1	244	13	3.8
0.9	3.1	733	27	46	5.9	23	4.5	1.0	4.0	0.6	4.0	0.8	2.6	0.4	3.1	0.6	15.4	0.9	23	12	3.9
0.7	1.6	856	25	44	5.5	22	4.5	1.0	4.3	0.7	5.4	1.4	5.5	1.0	8.7	1.6	123.6	1.0	9	12	10.5
0.6	2.5	742	27	57	6.5	26	4.8	2.0	6.5	1.0	4.6	1.0	3.7	0.6	4.0	0.6	14.6	1.6	109	8	7.4
1.4	3.3	751	35	70	8.2	31	5.6	1.8	6.9	1.0	4.2	0.9	2.9	0.4	3.2	0.5	13.0	1.0	93	14	4.1
1.1	2.5	593	19	39	4.3	15	2.9	1.7	3.9	0.7	2.4	0.5	1.7	0.2	1.7	0.3	10.1	0.7	6	7	3.4
1.0	2.7	752	18	43	4.6	15	2.9	1.9	3.9	0.6	2.4	0.6	2.0	0.3	2.5	0.4	14.9	0.7	7	6	3.4
1.1	4.0	1182	20	48	4.8	17	2.9	1.0	2.5	0.4	2.2	0.5	1.4	0.2	1.7	0.3	8.9	0.8	8	7	5.5
2.1	4.9	808	20	59	5.1	18	3.6	1.0	3.3	0.6	4.0	0.8	2.5	0.3	3.3	0.4	9.5	1.0	18	18	8.2
0.5	2.7	744	17	36	3.9	14	2.9	0.8	2.7	0.4	3.0	0.7	2.5	0.4	4.0	0.7	18.2	0.7	4	8	8.4
0.8	1.9	714	26	50	6.2	24	4.6	1.0	3.8	0.5	3.2	0.7	2.2	0.4	3.1	0.5	18.1	0.9	5	9	9.5
1.2	4.8	1368	35	69	8.4	32	5.8	2.1	6.7	1.0	4.2	0.9	3.4	0.5	3.7	0.6	18.2	1.6	26	18	3.2
0.7	2.7	960	35	70	8.1	31	6.0	1.3	5.8	1.0	6.9	1.4	4.3	0.7	5.4	0.7	12.6	1.1	830	13	5.7
0.5	2.0	601	30	64	7.0	27	4.7	1.1	3.7	0.5	3.5	0.7	2.3	0.4	3.5	0.5	14.6	1.6	836	9	3.4
0.9	1.7	1020	33	52	6.9	28	5.2	1.0	5.1	0.8	5.3	1.3	3.8	0.7	3.8	0.7	9.4	1.2	4	15	9.0
1.2	1.1	1084	35	57	7.3	28	5.9	1.0	5.9	0.9	6.0	1.4	4.4	0.6	4.9	0.7	8.7	1.2	4	14	12.0
1.0	0.8	1032	27	46	5.8	24	4.5	0.9	3.4	0.7	4.7	1.0	2.6	0.4	3.0	0.5	8.4	1.1	3	24	9.2
0.6	1.2	1213	29	50	6.0	25	4.4	1.1	4.9	0.7	5.0	1.2	3.6	0.5	3.7	0.7	6.7	0.9	5	13	8.8
	0.8	1039	29	48	5.8	25	4.5	1.0	3.9	0.6	3.7	0.9	2.2	0.4	2.9	0.5	6.6	1.1	3	11	8.5
0.8	0.9	1149	34	55	7.6	31	6.1	1.2	5.5	1.0	6.2	1.4	3.8	0.6	4.7	0.8	10.8	1.0	7	14	12.9
1.4	2.1	1162	31	51	6.2	26	5.0	1.0	4.3	0.7	4.5	1.1	3.1	0.4	3.4	0.6	8.0	1.1	4	11	10.3
2.3	6.0	1797	39	69	8.3	35	5.9	1.4	5.6	0.9	5.8	1.2	2.9	0.5	3.4	0.6	7.0	1.3	25	17	15.4
1.8	5.0	796	30	66	7.2	26	4.5	1.0	3.5	0.5	3.2	0.6	2.2	0.3	2.7	0.4	8.9	0.8	14	11	4.8
1.6	3.2	810	28	66	7.1	26	4.8	1.2	3.4	0.5	2.5	0.5	1.6	0.3	2.1	0.3	8.4	0.7	10	6	2.1
0.8	2.2	731	24	51	5.3	21	4.1	0.9	3.6	0.5	3.2	0.7	2.2	0.4	3.0	0.5	9.5	0.9	5	9	2.9
0.8	1.2	782	25	44	5.5	22	4.4	1.0	4.1	0.6	4.1	0.8	2.3	0.4	2.7	0.4	5.5	1.3	7	9	12.0
0.4	1.1	612	19	32	4.1	17	3.1	0.7	2.9	0.5	2.9	0.6	1.9	0.3	2.0	0.3	4.1	0.9	8	7	11.2
3.1	3.2	753	30	54	6.8	26	4.9	1.0	4.2	0.6	3.7	0.8	2.3	0.3	2.6	0.3	4.3	1.0	317	12	3.8
0.8	1.4	723	22	45	5.4	22	3.8	0.9	3.4	0.5	3.0	0.6	1.7	0.3	1.8	0.3	3.7	1.1	6	8	7.0
1.0	3.2	648	35	66	7.7	28	5.6	2.0	7.7	1.2	5.9	1.1	3.8	0.4	2.7	0.4	3.3	0.9	65	10	3.4
0.7	2.4	764	25	54	6.5	23	4.8	1.9	6.1	0.8	3.5	0.7	2.4	0.3	2.1	0.3	7.7	0.9	57	8	3.1
0.9	2.9	674	24	48	5.6	21	4.1	1.5	5.2	0.8	3.0	0.6	2.2	0.3	2.1	0.3	4.2	0.8	88	7	3.2
1.1	2.9	540	34	69	8.0	29	5.5	1.5	6.6	0.9	3.9	0.8	2.8	0.4	2.9	0.4	10.2	1.0	70	12	5.4
3.4	2.9	1052	27	55	6.3	23	5.0	2.1	6.5	0.8	3.2	0.7	2.7	0.3	2.4	0.4	4.7	1.2	122	9	4.9
3.4	1.9	800	20	36	4.5	17	3.0	1.3	4.0	0.6	2.9	0.6	2.0	0.3	2.5	0.3	6.2	0.6	88	9	3.9
2.6	2.0	861	26	51	6.3	22	4.3	1.6	4.8	0.7	2.9	0.6	2.1	0.2	1.9	0.2	3.9	0.9	107	8	6.0
2.5	1.5	567	20	41	5.1	16	3.1	1.2	3.1	0.5	2.0	0.4	1.2	0.2	1.4	0.2	3.9	0.7	263	5	3.8
2.6	1.7	625	19	39	4.8	16	2.9	1.3	3.7	0.6	2.5	0.5	1.8	0.3	2.2	0.3	3.6	0.6	292	5	3.7
1.3	1.9	466	28	58	6.6	27	5.8	1.9	8.7	1.3	4.1	0.9	3.1	0.3	2.8	0.3	1.5	0.8	30	7	5.5
0.8	0.6	850	23	51	5.6	19	3.8	3.0	5.3	0.8	2.4	0.5	2.1	0.2	1.8	0.3	3.8	1.0	4	11	10.4
0.5	1.3	648	33	46	5.8	28	5.8	2.2	7.3	1.1	4.4	0.9	3.4	0.4	3.5	0.5	8.2	1.6	3	13	8.3
1.9	7.1	820	12	24	2.3	6	0.7	1.2	1.3	0.2	0.7	0.2	0.7	0.1	0.6	0.1	1.2	0.2	14	5	15.8
0.7	1.5	666	24	44	5.5	21	3.7	0.9	3.1	0.5	2.9	0.6	1.7	0.3	1.8	0.3	4.9	0.7	4	8	3.4
1.0	0.6	584	45	84	11.7	43	8.1	2.4	9.9	1.4	5.1	0.9	3.4	0.4	3.0	0.5	8.3	0.7	46	10	15.4
0.6	2.8	798	23	45	5.4	22	4.1	1.6	5.0	0.7	3.3	0.6	2.3	0.3	2.6	0.3	9.0	0.8	7	8	3.9
0.7	1.7	700	43	81	10.1	38	6.7	1.6	8.0	1.1	4.2	0.8	2.9	0.3	2.7	0.3	5.1	0.9	55	12	4.4
0.9	2.7	727	22	43	5.4	22	4.1	1.4	5.0	0.7	3.3	0.6	2.2	0.3	2.2	0.3	5.8	0.9	13	8	3.4
0.8	2.4	818	26	51	6.3	25	4.8	1.7	5.6	0.8	3.6	0.7	2.4	0.3	2.4	0.3	5.2	0.8	16	9	4.6
0.9	3.1	609	19	46	4.7	16	3.3	1.3	5.5	1.0	7.0	1.5	4.1	0.5	3.2	0.5	3.9	0.8	7	7	4.6
0.9	3.4	686	20	41	4.7	18	3.4	1.2	4.4	0.7	3.0	0.7	2.2	0.3	2.5	0.4	7.1	0.7	7	9	5.0
1.2	3.0	655	28	49	6.1	24	4.8	1.4	6.2	1.0	5.1	1.1	3.6	0.5	3.8	0.6	5.2	1.1	11	13	4.0
1.6	3.2	823	31	69	7.6	27	4.7	1.1	4.3	0.7	4.1	0.8	2.6	0.4	2.9	0.4	6.1	0.9	1217	11	3.3
1.1	0.9	419	16	30	3.6	13	2.3	0.5	1.9	0.3	1.7	0.3	1.2	0.1	1.1	0.2	3.3	0.4	206	5	3.7
0.9	0.8	387	15	28	3.3	12	2.0	0.5	1.7	0.2	1.5	0.3	0.9	0.2	1.1	0.2	2.6	0.4	173	4	3.6
0.8	1.1	483	18	34	4.1	14	2.8	0.6	2.1	0.3	2.0	0.3	1.2	0.2	1.3	0.2	3.6	0.5	201	5	3.8

(continued on next page)

Table 3 (*continued*)

Sample number	Distance[a]	1σ[a]	FeO	MnO	Na_2O	Al_2O_3	MgO	SiO_2	TiO_2	K_2O	CaO	Sum	Cr[b]	Co	Cu	Ga	Rb	Sr	Y	Zr	Nb
U-enriched n = 44																					
4f-2.36b-4			2.2	0.089	1.4	9.0	0.9	75.4	0.38	2.7	6.0	98.0	21	4.2	7.6	6.3	42	143	11	40	11.5
4f-2.36b-8			5.2	0.081	1.4	17.7	1.0	55.1	0.53	1.6	14.1	96.7	23	7.0	55.4	4.4	48	327	22	50	14.5
4f-2.36b-9			2.0	0.019	1.8	12.9	0.8	67.5	0.34	3.5	7.5	96.3	13	3.8	17.4	7.2	100	188	11	55	7.2
4F-5.37-06	51	4	2.5	0.068	0.9	17.1	1.2	55.8	0.46	2.6	18.2	98.9	17	2.0	3.9	4.0	101	449	18	96	8.0
4F-5.37-08	51	4	2.5	0.012	0.9	12.3	1.0	62.2	0.34	1.6	18.0	98.9	12	1.7	3.2	2.3	30	358	18	98	7.1
4F-5.37-12	51	4	1.8	0.034	1.4	13.8	0.8	62.3	0.40	3.0	14.3	97.8	27	1.5	3.4	2.6	45	371	20	115	8.1
4F-5.37-13	51	4	2.3	0.068	0.9	14.6	1.1	57.6	0.39	1.7	20.5	99.1	6	1.1	2.6	1.7	25	231	11	66	4.5
5A-6.06-1	51	2	2.9	0.057	1.5	18.4	1.1	54.4	0.38	2.9	17.7	99.3	14	3.1	9.6	2.3	94	480	21	101	8.0
5A-6.06-2	51	2	2.4	0.072	1.4	10.8	0.9	58.9	0.25	1.8	22.9	99.4	20	4.3	9.4	6.8	70	486	19	104	7.2
5A-6.06-3	51	2	1.5	0.041	1.2	8.6	0.7	68.2	0.22	2.5	16.3	99.3	18	1.7	5.5	4.2	79	376	16	88	7.8
5A-6.06-6	51	2	2.5	0.034	1.6	14.5	1.2	62.2	0.40	2.2	14.0	98.7	16	2.4	4.8	4.4	57	358	18	88	8.0
5b-10.4b-03	58	5	2.8	0.049	2.3	14.5	1.0	68.6	0.54	3.5	7.1	100.3	37	7.0	11.8	13.8	157	343	31	86	13.5
5d-1.72b-02	74	7	3.0	0.066	1.5	13.2	1.3	66.2	0.72	2.8	9.3	98.1	23	4.5	9.4	8.5	91	248	36	106	14.5
5d-1.72b-07	74	7	2.5	0.022	1.9	22.8	1.3	53.3	0.55	1.6	14.7	98.6	18	3.7	22.4	8.1	48	391	20	113	19.0
Non-enriched n = 38																					
1-3.59a-09			2.2	0.054	1.8	13.1	0.9	65.7	0.34	3.8	8.3	96.1	30	5.8	14.9	11.8	136	212	12	33	8.1
1-3.59a-11			7.5	0.085	0.9	14.2	1.9	56.7	0.75	1.7	13.3	97.1	41	7.5	9.2	7.6	84	329	19	51	10.6
3-5.2a-05			2.2	0.077	2.6	14.3	1.0	65.0	0.45	3.4	7.3	96.3	23	7.0	60.3	8.6	103	220	14	22	7.9
3-5.2a-07			3.0	0.068	1.4	12.4	1.5	67.5	0.57	2.1	9.3	97.8	58	9.5	160.2	13.3	113	273	17	72	10.8
4a-1.95a-01			3.0	0.129	1.9	15.3	1.4	62.3	0.73	3.0	9.3	97.1	37	6.5	16.0	5.8	74	177	13	68	8.3
4a-1.95a-05			1.7	0.021	1.0	11.0	0.8	73.0	0.38	4.2	5.3	97.5	13	4.7	8.0	4.9	115	137	6	21	5.0
4a-1.95a-09			3.2	0.043	2.4	12.5	1.2	61.6	0.58	2.7	9.0	93.3	12	5.6	28.5	3.3	23	78	6	15	2.4
4a-1.95a-13			2.7	0.049	1.8	10.7	0.9	63.1	0.43	2.8	15.0	97.5	22	10.1	97.8	8.1	50	167	15	17	6.1
4b-2.64b-01	55	6	2.8	0.025	1.8	11.4	1.0	69.9	0.51	2.9	6.7	97.0	23	7.7	4.2	4.9	54	124	6	22	4.7
4c-10.6a-05	67	5	2.5	0.023	1.7	11.3	1.0	69.9	0.81	3.2	7.0	97.5	40	5.9	29.7	15.8	105	210	16	54	11.8
4c-10.6a-06	67	5	2.7	0.070	1.9	14.3	1.1	65.8	0.65	3.1	7.2	97.0	30	6.5	33.5	12.7	114	245	16	46	14.3
4c-10.6a-07	67	5	2.4	0.049	2.0	13.5	0.9	67.5	0.43	3.4	7.6	97.8	29	5.5	48.4	14.8	122	225	13	77	9.9
4c-10.6a-10	67	5	1.6	0.092	2.4	16.1	0.5	67.9	0.19	4.9	4.5	98.2	21	4.3	17.8	12.8	328	187	4	66	2.8
4d-9.18a-01	68	7	0.9	0.043	0.6	3.8	0.8	64.3	0.14	0.7	26.3	97.5	27	7.5	34.4	7.6	136	201	19	91	10.6
4d-9.18a-02	68	7	2.2	0.036	1.6	13.1	0.9	69.3	0.40	4.2	7.5	99.2	28	5.9	28.7	6.3	116	184	17	59	9.4
4d-9.18a-04	68	7	2.0	0.026	1.9	12.4	0.8	70.2	0.40	3.5	6.6	97.8	18	10.6	12.4	2.7	20	481	7	28	2.3
4d-9.18a-05	68	7	3.4	0.056	0.4	11.8	1.4	49.5	0.51	0.8	29.8	97.8	20	12.9	16.6	3.3	20	576	7	7	2.1
4d-9.18a-06	68	7	1.2	0.008	0.7	6.3	1.0	64.6	0.28	1.2	22.7	98.0	38	10.1	18.5	11.9	118	313	19	27	12.9
4d-9.18a-08	68	7	3.1	0.121	1.9	14.6	1.5	65.2	0.62	2.8	8.8	98.6	25	6.3	44.3	7.0	106	194	16	63	8.7
4e-5.22b-01	60	7	1.9	0.050	2.4	12.5	0.8	70.3	0.35	3.4	5.8	97.5	27	5.7	7.8	6.9	97	234	15	45	8.6
4e-5.22b-02	60	7	2.9	0.072	2.4	13.9	1.1	67.7	0.49	3.6	7.2	99.3	34	8.1	11.1	11.7	104	225	27	57	12.5
4e-5.22b-04	60	7	2.3	0.000	1.5	14.2	1.1	69.0	0.48	2.1	7.4	98.1	17	5.6	4.2	2.2	74	250	19	67	11.0
4e-5.22b-05	60	7	2.5	0.044	3.2	14.7	1.1	65.7	0.81	3.5	7.3	99.0	30	8.0	10.2	10.3	127	230	13	39	11.2
4f-2.36a-06			1.6	0.050	2.2	16.6	0.5	65.3	0.20	5.8	4.2	96.6	23	3.4	58.6	9.4	141	290	8	29	7.9
4f-2.36a-07			1.7	0.056	1.9	15.8	0.7	66.9	0.46	4.0	5.4	97.0	17	3.8	15.5	6.6	148	211	8	22	10.2
4f-2.36a-09			2.2	0.068	1.6	11.0	1.0	69.2	0.44	3.6	6.8	96.0	66	5.9	35.8	8.8	92	193	12	23	8.5
4f-2.36b-7			0.8	0.000	2.0	18.2	0.3	64.9	0.01	7.9	3.9	98.1	13	3.5	14.2	6.3	110	115	9	15	6.8
5A-6.06-7	51	2	3.1	0.059	2.3	11.9	3.0	64.4	0.45	2.7	10.5	98.3	113	1.8	3.0	7.4	69	216	5	8	3.7
5b-10.4b-01	58	5	2.1	0.053	1.9	10.5	0.9	74.6	0.41	3.4	5.5	99.4	25	5.9	7.3	11.0	200	240	15	115	9.4
5b-10.4b-02	58	5	2.3	0.039	1.7	9.5	0.9	75.6	0.42	3.2	5.5	99.3	42	4.3	6.1	7.9	77	226	10	54	7.8
5b-10.4b-06	58	5	1.5	0.017	2.0	11.7	0.7	73.6	0.30	5.0	4.6	99.4	22	4.3	7.2	10.4	170	145	6	20	5.4
5b-10.4b-08	58	5	1.1	0.000	2.2	16.4	0.3	68.5	0.19	6.7	2.9	98.2	12	2.4	4.9	6.0	92	106	5	14	6.0
5b-10.4b-09	58	5	2.7	0.013	2.2	16.0	1.1	64.0	0.37	3.4	7.8	97.5	31	4.8	7.6	17.0	124	299	9	27	5.7
5b-10.4b-10	58	5	2.2	0.046	1.5	12.8	0.9	70.3	0.50	3.6	6.6	98.5	20	4.5	9.6	4.3	142	195	11	46	7.5
5d-1.72b-01	74	7	6.9	0.043	2.6	14.7	0.8	62.5	0.32	3.3	7.1	98.4	81	9.6	12.4	13.0	76	199	13	38	8.6
5d-1.72b-05	74	7	2.6	0.040	1.8	13.2	1.1	68.9	0.47	3.0	7.9	99.1	35	5.0	10.0	8.9	89	211	14	84	10.4
5d-1.72b-06	74	7	3.4	0.084	2.3	14.5	1.6	64.7	0.47	3.3	8.6	98.9	33	6.1	14.8	10.7	90	409	10	39	9.1
5d-1.72b-08	74	7	2.6	0.054	1.7	12.7	1.1	67.1	0.52	2.8	8.3	96.8	22	4.7	5.1	5.8	69	206	13	48	10.4
K-feldspar, 4E-5.22b			0.09	0.008	0.88	18.25	0.00	64.2	0.07	15.45	0.02	98.932									
Average from the triplicate analyses of un-melted sand													27	5.0	26	6.8	144	185	18	216	10.0

[a] Calculated distances and 1σ uncertainty from ground zero are from Bellucci et al. (2013a).
[b] After Cr all trace elements are reported in mg/g.

ratio in ilmenite is constant. The fractionation in the ratio between metals could be the result of mixing with Fe and other metals from the steel bomb tower. Enrichments in CaO are likely due to the incorporation of calcite, gypsum, or plagioclase, which are present as natural components in the sand. Abundances of Na_2O or SiO_2 vs. FeO do not define any trends, and are likely the result of mixing of quartz, K-feldspar, plagioclase, and chlorites. Trends in the abundances of K_2O vs. FeO are the most apparent, and are presumably due to variable mixing between K-feldspar, non-K- or Fe-bearing phases, and the FeO-rich anthropogenic component. Of note, there are no trends observed between the abundances of the major elements and the calculated distance away from ground zero (based on the activity of ^{152}Eu; Bellucci et al., 2013a).

5.2. Determining end-member phases

The variation in abundances of several trace elements analyzed (i.e., Ba, Sr, Rb, Nb, Ta) can be attributed to mixing between major and minor phases present in the arkosic sand (Fig. 4). In contrast to the majority of elements investigated here, the concentrations of Ba are the most consistent, and suggest that Ba is most likely buffered by the presence of barite originally present in the sand; hence, any additions from the Baratol present in Gadget are not resolvable. The concentration of Sr in trinitite is dependent on the relative amount of mixing between calcite and/or gypsum (Sr-rich end-members) and K-feldspar and quartz (Sr-poor end-members) as shown in Fig. 4.

Sn	Cs	Ba	La	Ce	Pr	Nd	Sm	Eu	Gd	Tb	Dy	Ho	Er	Tm	Yb	Lu	Hf	Ta	Pb	Th	U
0.7	1.7	423	21	47	5.0	17	3.0	0.6	2.3	0.4	1.8	0.4	1.2	0.2	1.4	0.2	2.5	0.6	1289	8	3.6
0.5	1.0	807	37	33	5.7	32	6.7	1.5	5.2	0.7	4.4	0.8	2.2	0.3	2.5	0.3	2.9	1.5	329	13	44.8
1.0	2.7	760	17	35	3.9	14	2.3	0.6	2.0	0.3	1.8	0.4	1.1	0.2	1.4	0.2	3.3	0.6	50	6	7.2
	2.7	1031	23	34	4.8	18	3.4	0.9	3.2	0.5	2.9	0.6	1.7	0.3	1.9	0.3	4.6	0.7	3	10	6.6
	0.8	715	20	32	3.9	16	3.0	0.7	2.7	0.5	3.0	0.7	1.8	0.3	1.9	0.3	4.9	0.6	1	11	8.6
	1.2	646	23	30	4.6	19	4.0	0.7	3.2	0.4	3.1	0.7	2.0	0.3	2.3	0.3	5.3	0.8	3	10	6.7
	0.8	479	13	20	2.8	11	2.2	0.5	2.0	0.3	2.0	0.4	1.2	0.2	1.1	0.2	3.1	0.5	1	6	4.1
1.6	2.3	1090	26	46	5.7	23	4.4	1.1	4.1	0.7	3.8	0.6	2.2	0.3	2.5	0.4	5.3	0.8	9	12	12.2
<0.58	2.0	785	23	40	4.9	19	4.0	0.9	3.9	0.4	3.2	0.7	2.2	0.3	2.1	0.3	5.4	0.6	5	15	5.4
<0.77	2.0	658	24	41	5.1	22	3.6	0.7	3.2	0.5	3.0	0.6	1.6	0.2	1.4	0.2	4.5	0.8	9	12	4.6
1.1	1.3	627	23	35	4.9	20	3.8	0.7	3.2	0.5	3.2	0.7	1.6	0.3	2.2	0.3	4.5	1.0	4	13	6.7
2.0	4.8	1072	31	70	7.5	27	5.1	1.2	4.4	0.8	4.9	1.1	3.3	0.6	4.4	0.6	4.6	1.1	12	10	5.4
1.9	3.1	829	22	48	5.5	20	4.0	1.0	4.0	0.7	4.6	1.1	3.3	0.6	4.2	0.6	5.1	0.9	17	7	4.4
0.9	1.2	997	32	46	7.5	26	4.7	1.2	3.7	0.6	3.4	0.7	2.1	0.3	2.7	0.3	6.4	1.8	4	11	5.8
1.8	4.4	956	19	45	4.5	17	2.8	0.8	2.3	0.3	2.1	0.4	1.3	0.2	1.3	0.2	2.5	0.6	72	7	1.6
1.1	2.6	978	28	48	6.0	25	4.5	1.1	4.3	0.6	3.5	0.7	2.1	0.3	2.2	0.3	3.3	0.9	17	8	2.7
1.0	4.6	617	20	47	4.6	16	3.0	1.4	3.8	0.6	2.4	0.5	1.6	0.2	1.6	0.2	2.0	0.6	53	5	1.8
1.1	3.7	1071	25	45	5.9	23	4.3	1.8	5.2	0.8	3.4	0.6	1.8	0.2	2.1	0.3	6.2	0.7	168	7	2.8
6.8	2.2	694	19	34	3.7	14	2.9	1.4	3.8	0.6	2.4	0.5	1.7	0.2	1.7	0.3	7.2	0.8	241	8	1.4
1.9	3.4	497	12	24	2.8	9	1.8	0.9	2.3	0.3	1.4	0.2	0.8	0.1	0.8	0.1	2.1	0.4	3	4	1.4
2.2	0.9	216	6	11	1.5	6	1.6	0.5	1.5	0.2	1.1	0.2	0.9	0.1	0.6	0.1	1.6	0.1	70	2	0.6
1.4	1.7	460	19	35	4.7	17	3.3	1.2	4.1	0.7	2.9	0.5	1.9	0.2	1.5	0.2	1.7	0.4	247	2	1.5
2.3	1.4	437	10	20	2.2	9	1.7	2.6	2.9	0.5	1.2	0.2	1.1	0.1	0.8	0.1	2.1	0.3	7	3	0.9
1.7	3.5	800	67	165	15.1	48	6.3	1.1	4.5	0.6	3.0	0.6	1.7	0.3	1.9	0.3	3.0	0.8	11	13	2.9
1.1	3.8	765	19	47	4.9	18	3.1	0.9	2.5	0.4	2.9	0.6	1.7	0.2	2.0	0.2	2.3	0.8	11	7	2.1
2.1	3.8	762	20	54	6.0	21	4.0	1.1	3.1	0.4	2.6	0.4	1.3	0.2	1.5	0.2	4.2	0.7	16	6	2.7
1.9	11.1	1126	4	13	1.1	4	0.6	0.5	0.5	0.1	0.5	0.2	0.3	0.1	0.6	0.1	3.6	0.2	26	2	1.7
1.5	3.4	682	29	54	6.2	24	4.3	1.5	5.7	0.8	3.2	0.7	2.5	0.3	2.5	0.3	9.1	0.8	14	12	2.8
1.0	2.9	601	25	47	5.6	22	3.7	1.2	5.0	0.7	3.3	0.6	2.1	0.3	2.1	0.3	5.7	0.7	36	10	2.4
0.7	0.9	425	9	16	2.2	8	1.6	0.7	2.0	0.3	1.2	0.2	0.8	0.1	0.7	0.1	3.6	0.2	7	3	3.0
1.1	0.8	224	8	13	2.0	7	1.4	0.5	2.0	0.3	1.2	0.3	0.9	0.1	0.7	0.1	0.9	0.2	11	2	2.5
1.3	3.8	836	35	65	7.6	28	5.0	1.9	6.2	0.9	3.4	0.6	2.3	0.2	2.1	0.3	2.9	0.9	116	10	2.2
1.0	2.9	669	22	41	4.8	19	3.4	1.2	4.4	0.6	2.9	0.6	2.0	0.3	2.0	0.3	5.8	0.8	7	9	2.3
1.0	3.0	621	22	42	5.0	19	3.6	1.2	4.6	0.6	2.6	0.5	2.0	0.2	1.8	0.3	4.7	0.7	8	8	2.6
1.5	3.0	621	18	39	4.5	16	3.3	1.4	4.6	0.7	4.2	0.9	3.3	0.4	3.4	0.5	5.0	1.0	12	6	2.0
0.4	1.6	888	27	52	6.0	24	4.6	1.7	5.3	0.8	3.1	0.7	2.3	0.3	2.2	0.4	6.5	1.0	3	10	2.8
1.0	4.3	831	22	42	5.0	19	3.6	1.7	4.4	0.7	2.4	0.5	1.7	0.2	1.4	0.2	3.6	0.7	10	7	2.2
0.9	3.0	1692	18	26	2.9	10	1.9	0.6	1.5	0.3	1.4	0.3	0.8	0.1	1.0	0.1	1.8	0.6	1510	1	1.8
1.3	4.0	883	15	31	3.3	12	2.0	0.5	1.8	0.2	1.6	0.3	0.9	0.1	1.0	0.1	1.3	0.7	1115	6	2.8
0.9	3.0	788	21	48	5.2	18	3.4	0.8	2.6	0.4	2.2	0.4	1.3	0.2	1.3	0.2	1.4	0.6	1735	5	1.5
0.9	1.8	781	13	26	3.1	12	2.4	0.6	2.1	0.3	1.6	0.3	0.9	0.1	1.1	0.1	1.0	0.4	450	4	2.0
0.4	2.1	291	8	14	1.8	7	1.2	0.3	1.0	0.1	0.9	0.2	0.5	0.1	0.5	0.1	0.4	0.4	6	2	0.3
3.7	6.7	1014	27	49	5.2	17	3.2	0.9	3.2	0.4	2.8	0.5	1.7	0.2	1.8	0.3	5.0	0.5	16	7	2.0
1.9	2.4	628	15	36	3.7	13	2.3	0.7	1.8	0.3	1.8	0.4	1.0	0.2	1.4	0.2	2.8	0.5	7	5	2.8
1.9	5.1	580	10	23	2.4	8	1.4	0.5	1.2	0.2	1.0	0.2	0.6	0.1	0.8	0.1	1.2	0.3	13	4	1.4
0.8	2.2	456	13	30	3.0	10	1.7	0.4	1.2	0.2	0.8	0.2	0.5	0.1	0.5	0.1	0.9	0.4	8	4	0.9
1.2	3.3	661	17	36	4.0	15	2.7	1.0	2.3	0.3	1.9	0.3	0.9	0.1	1.1	0.1	1.7	0.4	8	6	1.6
1.9	3.6	973	17	34	3.7	14	2.4	0.8	2.1	0.4	1.8	0.4	1.1	0.2	1.2	0.2	2.6	0.7	8	6	1.3
2.3	2.5	501	14	31	3.5	13	2.5	0.8	2.3	0.3	2.1	0.4	1.4	0.2	1.7	0.2	2.3	0.5	16	10	2.9
1.0	3.1	708	25	52	5.6	20	3.8	0.8	2.8	0.4	2.5	0.5	1.4	0.2	1.7	0.3	4.9	0.7	6	9	2.2
1.8	3.2	297	13	37	4.1	15	2.9	0.8	2.3	0.3	1.9	0.3	1.0	0.2	1.1	0.1	2.3	0.6	10	6	1.2
1.0	2.2	716	24	49	5.4	20	3.4	0.8	2.8	0.4	2.3	0.4	1.3	0.2	1.5	0.2	2.9	0.7	4	7	1.9
2.5	4.2	687	23	47	5.2	20	3.7	0.7	2.8	0.4	3.0	0.6	1.8	0.3	2.0	0.3	5.4	1.5	41	10	3.2

Rubidium contents define a positive correlation with K_2O abundances, which suggests that the Rb budget in trinitite glass is determined by the amount of K-feldspar present during melting. Niobium and Ta, which are geochemical surrogates, correlate with TiO_2 contents and suggest that ilmenite may be largely responsible for the budget of these elements. Two data points do not fall on the main trend and display gross enrichments in both Nb and Ta (Fig. 4). These data points cannot be explained by the presence of an additional natural mineral phase and therefore, could likely have an anthropogenic origin. A Ta-bearing inclusion has previously been reported on the surface of trinitite, and could be attributed to either the tamper or electronics used in the device and hence may have served as the carrier for both Nb and Ta (Bellucci and Simonetti, 2012).

5.3. Trace elements

5.3.1. Trace element patterns

One of the most important aspects of this study is to attempt to resolve the exact origin of the trace elements, whether these emanate from the blast site (or device), or derive from the sand (natural background). Moreover, temperature-induced fractionation of the elemental abundances/ratios as a result of the explosion could have occurred due to the extreme heat. Therefore, normalizing trace element concentrations to those for the un-melted sand, and ordering them by decreasing condensation temperature (50% T_C (K), Lodders, 2003) should yield much information (Fig. 5). As with the trends defined by the major element abundances (Fig. 3), the contents of the trace elements

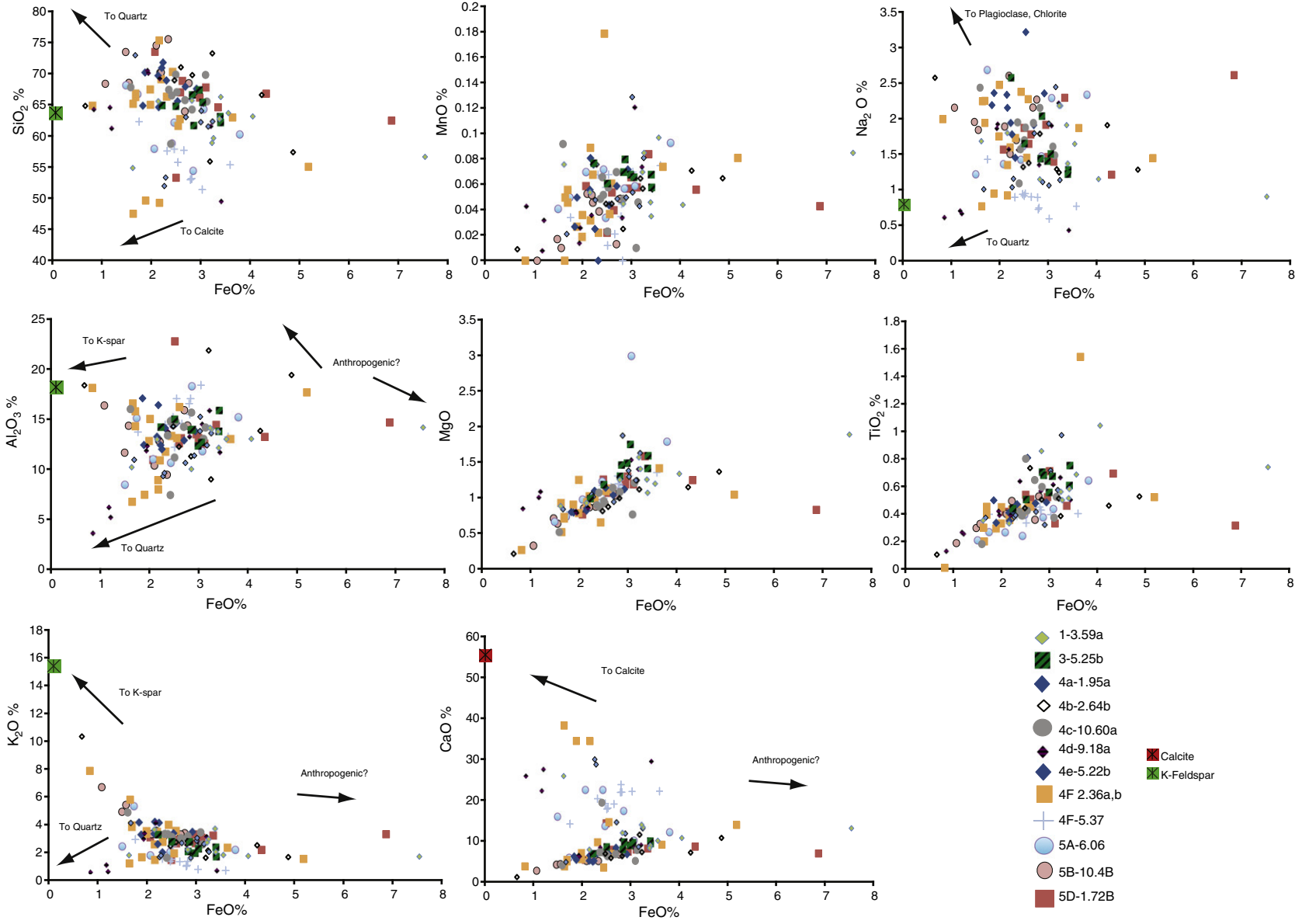

Fig. 3. Major elements plotted against FeO. All units are in wt.%.

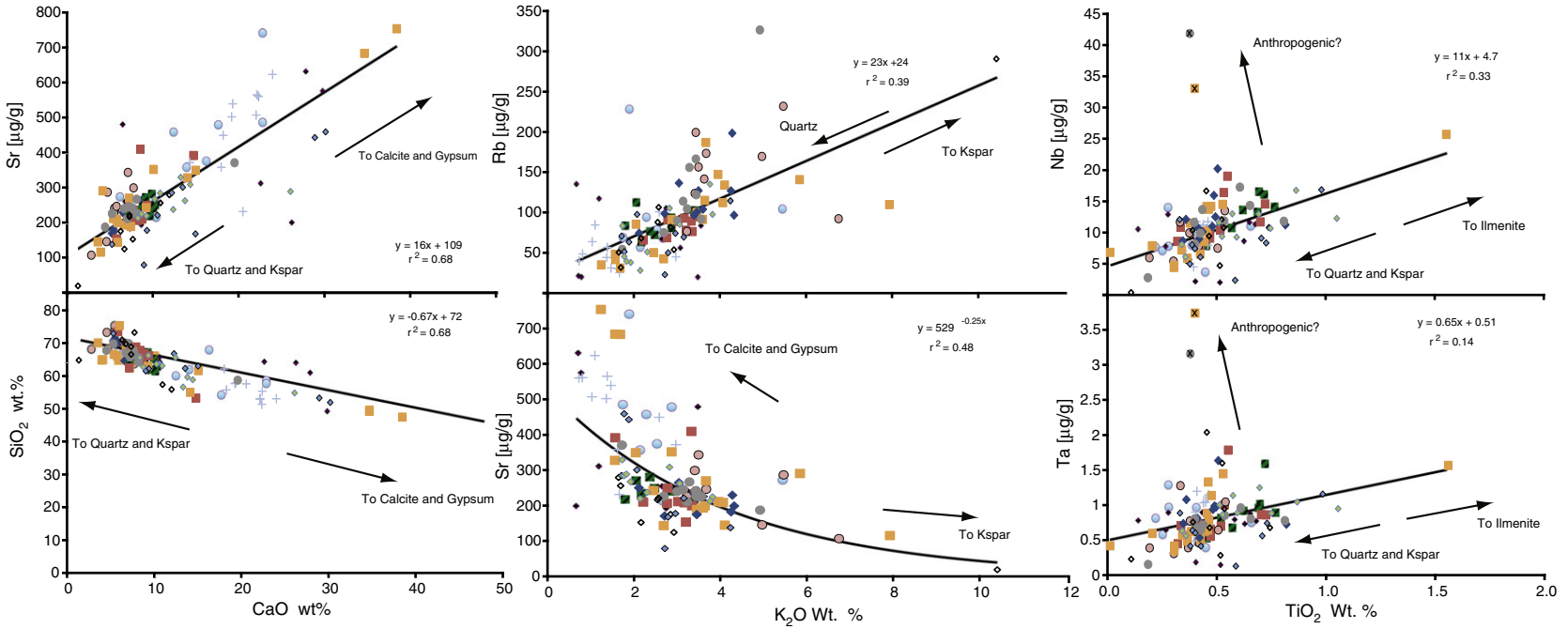

Fig. 4. Major and trace element diagrams indicating mixing between phases. Data marked with an x are not included in linear regression calculations.

Table 4
Basic statistics for each sample and whole dataset.

Sample number		FeO	MnO	Na_2O	Al_2O_3	MgO	SiO_2	TiO_2	K_2O	CaO	Cr[a]	Co	Cu	Ga	Rb	Sr	Y	Zr	Nb	Sn
1-3.59a	Average	3.5	0.06	1.6	12.8	1.3	61.8	0.6	2.5	12.7	32.8	5.4	15.3	7.3	70.9	262.9	22.3	235.9	11.0	1.3
n = 10	1σ	1.6	0.02	0.4	1.5	0.3	4.0	0.2	0.8	5.1	20.0	1.2	14.1	3.5	35.7	39.6	8.0	510.4	3.0	0.9
	1σ%	45%	34%	28%	12%	23%	6%	35%	32%	40%	61%	21%	92%	47%	50%	15%	36%	216%	27%	68%
	Maximum	7.5	0.10	2.2	14.2	1.9	66.3	1.0	3.8	26.0	86.8	7.5	49.5	12.6	135.5	328.7	41.5	1682.2	16.7	3.1
	Minimum	1.6	0.04	0.9	10.1	0.9	54.9	0.3	1.7	8.3	17.3	3.6	4.6	2.7	28.0	212.4	11.5	32.8	6.1	0.4
	Median	3.3	0.06	1.7	13.1	1.3	63.0	0.6	2.2	11.6	27.3	5.2	9.0	7.5	67.2	264.2	21.8	55.1	11.1	0.8
3-5.2a	Average	2.9	0.07	1.6	14.1	1.4	64.6	0.6	2.5	9.3	40.1	10.1	79.6	8.1	86.4	246.2	22.1	78.7	12.9	1.0
n = 8	1σ	0.4	0.01	0.5	1.1	0.2	2.0	0.1	0.5	1.1	14.3	2.1	106.5	3.1	16.4	22.5	6.5	44.9	2.9	0.2
	1σ%	14%	11%	28%	8%	17%	3%	17%	21%	11%	36%	21%	134%	39%	19%	9%	29%	57%	23%	24%
	Maximum	3.4	0.08	2.6	16.0	1.8	67.5	0.8	3.4	10.4	61.3	13.9	312.3	13.3	113.4	282.4	32.4	153.3	16.6	1.4
	Minimum	2.2	0.06	1.2	12.4	1.0	61.7	0.4	1.8	7.3	22.7	7.0	8.9	3.3	64.0	219.6	13.7	21.7	7.9	0.6
	Median	2.9	0.07	1.5	14.1	1.4	64.9	0.7	2.4	9.5	34.0	10.1	38.8	7.9	82.8	243.6	21.2	75.4	13.5	1.0
4a-1.95	Average	2.7	0.06	1.4	12.0	1.3	62.1	0.5	2.6	14.9	40.3	10.5	29.7	5.6	68.2	251.7	13.3	40.1	8.3	3.0
n = 9	1σ	0.5	0.03	0.5	2.0	0.3	6.4	0.2	0.8	8.8	38.7	4.3	27.4	1.4	26.9	131.9	4.7	19.6	4.2	1.6
	1σ%	19%	51%	37%	17%	27%	10%	40%	32%	59%	96%	41%	92%	25%	39%	52%	35%	49%	50%	53%
	Maximum	3.3	0.13	2.4	15.3	1.9	73.0	1.0	4.2	30.1	136.4	16.5	97.8	8.1	114.7	458.4	20.2	68.2	16.8	6.8
	Minimum	1.7	0.02	1.0	9.4	0.8	52.0	0.3	1.7	5.3	11.8	4.7	8.0	3.3	22.7	78.4	6.2	15.1	2.4	1.4
	Median	2.9	0.05	1.1	11.4	1.2	62.4	0.4	2.7	12.2	28.3	10.1	17.6	5.8	69.5	220.3	15.1	42.1	8.0	2.6
4b-2.64b	Average	3.0	0.05	1.6	15.1	1.0	66.0	0.5	3.4	7.4	34.6	7.7	7.9	5.0	96.5	180.0	14.6	67.7	9.4	1.3
n = 8	1σ	1.3	0.02	0.5	4.4	0.4	6.3	0.2	2.9	3.2	34.5	2.7	5.1	3.3	82.4	83.1	7.2	64.8	4.9	0.6
	1σ%	42%	45%	29%	29%	37%	10%	38%	86%	43%	100%	35%	64%	66%	85%	46%	49%	96%	52%	46%
	Maximum	4.9	0.07	2.6	21.9	1.4	73.4	0.7	10.4	11.9	117.4	10.3	19.0	12.1	291.8	278.5	25.6	198.2	16.6	2.3
	Minimum	0.7	0.01	1.2	9.1	0.2	55.9	0.1	1.7	1.3	9.2	1.3	4.2	1.7	31.6	18.6	5.1	6.2	0.4	0.5
	Median	3.0	0.05	1.4	14.1	1.1	67.8	0.5	2.6	7.3	23.6	8.5	6.0	4.3	75.0	195.3	13.9	50.6	10.5	1.2
4c-10.6a	Average	2.6	0.05	1.8	13.6	0.9	66.3	0.5	3.2	8.2	27.8	5.2	21.9	10.2	130.4	243.6	15.5	142.8	14.3	1.3
n = 10	1σ	0.4	0.02	0.4	2.5	0.2	3.2	0.2	0.8	4.2	7.9	1.3	12.9	5.2	77.4	49.3	5.1	120.0	10.4	0.6
	1σ%	17%	45%	21%	19%	21%	5%	36%	24%	51%	28%	26%	59%	51%	59%	20%	33%	84%	73%	48%
	Maximum	3.1	0.09	2.4	16.1	1.2	69.9	0.8	4.9	19.5	42.4	8.0	48.4	18.1	327.9	370.2	20.9	415.8	41.7	2.1
	Minimum	1.6	0.01	1.1	7.5	0.5	58.8	0.2	1.7	4.5	18.3	3.3	5.0	3.1	54.2	186.7	3.7	46.0	2.8	0.5
	Median	2.5	0.05	1.8	14.3	0.9	66.9	0.4	3.3	7.4	26.4	5.0	18.5	9.7	109.6	232.5	16.0	82.9	11.8	1.1
4d-9.18a	Average	2.2	0.05	1.3	11.1	1.1	64.5	0.4	2.4	15.0	29.2	9.5	21.8	6.1	75.2	323.8	17.9	54.9	9.0	1.0
n = 11	1σ	0.9	0.03	0.6	4.1	0.3	5.9	0.2	1.3	9.4	11.5	3.2	12.1	2.5	41.8	161.3	6.2	25.4	3.7	0.2
	1σ%	40%	69%	47%	37%	24%	9%	39%	54%	63%	39%	34%	55%	41%	56%	50%	35%	46%	41%	26%
	Maximum	3.4	0.12	2.2	16.0	1.5	70.6	0.7	4.2	29.8	60.5	17.0	44.3	11.9	136.2	631.8	29.0	90.7	12.9	1.5
	Minimum	0.9	0.01	0.4	3.8	0.8	49.5	0.1	0.7	6.6	18.3	5.9	7.5	2.7	20.3	183.6	7.3	7.5	2.1	0.6
	Median	2.2	0.04	1.6	12.4	1.1	65.2	0.4	2.8	9.4	25.9	9.1	18.5	6.3	79.6	256.5	18.8	57.7	10.6	1.0
4e-5.22b	Average	2.3	0.05	2.2	14.0	1.0	68.3	0.5	3.5	6.7	36.4	6.9	7.9	8.6	116.2	215.7	26.8	66.9	12.1	1.0
n = 10	1σ	0.3	0.03	0.5	1.7	0.1	2.6	0.1	0.7	1.1	20.8	1.1	2.1	3.3	34.5	32.6	15.8	47.0	3.5	0.3
	1σ%	15%	52%	22%	12%	14%	4%	28%	21%	16%	57%	16%	26%	39%	30%	15%	59%	70%	29%	28%
	Maximum	2.9	0.08	3.2	17.1	1.1	71.9	0.8	4.3	8.8	84.7	8.8	11.1	14.5	199.1	264.2	61.8	193.2	20.1	1.5
	Minimum	1.8	0.00	1.5	12.1	0.8	64.7	0.3	2.1	5.4	17.2	5.6	4.2	2.2	74.5	170.1	13.3	28.0	8.6	0.4
	Median	2.2	0.05	2.2	13.6	1.0	68.5	0.5	3.5	6.8	29.7	6.5	7.8	8.3	102.4	227.0	21.1	54.3	11.1	0.9
4f-2.36a,b	Average	2.3	0.05	1.7	13.0	0.9	62.7	0.4	3.3	12.5	30.6	5.2	29.6	7.5	92.1	314.6	15.2	66.3	11.9	1.0
n = 15	1σ	1.0	0.04	0.5	3.6	0.3	7.9	0.3	1.7	11.6	13.5	1.7	19.4	2.3	45.8	199.7	9.0	53.2	7.5	0.3
	1σ%	42%	81%	31%	27%	31%	13%	70%	51%	93%	44%	32%	65%	30%	50%	63%	59%	80%	63%	31%
	Maximum	5.2	0.18	2.5	18.2	1.4	75.4	1.6	7.9	38.4	65.7	9.0	74.4	13.3	187.5	752.8	44.1	191.2	33.0	1.6
	Minimum	0.8	0.00	0.8	6.8	0.3	47.5	0.0	1.2	3.6	13.4	3.4	7.6	4.4	31.0	114.9	8.2	14.5	4.4	0.5
	Median	2.2	0.05	1.8	13.2	0.9	65.1	0.4	3.5	7.3	27.4	4.4	22.1	7.4	91.5	242.1	11.5	49.6	10.2	0.9
4F-5.37	Average	2.7	0.04	0.9	15.3	1.2	56.3	0.4	1.5	20.2	19.9	2.5	6.7	2.7	51.8	478.3	26.8	146.2	9.4	1.0
n = 11	1σ	0.5	0.03	0.2	1.8	0.2	3.7	0.0	0.7	2.7	8.1	0.9	6.1	0.9	23.5	116.0	9.4	48.9	2.3	0.3
	1σ%	17%	58%	24%	12%	15%	7%	9%	46%	14%	41%	37%	92%	33%	45%	24%	35%	33%	24%	27%
	Maximum	3.6	0.08	1.4	18.5	1.4	62.3	0.5	3.0	23.9	32.8	4.2	24.5	4.7	101.0	622.6	38.3	232.2	11.7	1.4
	Minimum	1.8	0.00	0.6	12.3	0.8	51.4	0.3	0.7	14.3	6.4	1.1	2.6	1.7	25.2	230.9	11.4	66.5	4.5	0.6
	Median	2.7	0.05	0.9	15.3	1.2	55.8	0.4	1.4	20.5	18.8	2.4	4.9	2.6	44.9	506.3	26.1	148.2	10.2	1.0
5A-6.06	Average	2.5	0.06	1.8	13.2	1.3	61.6	0.4	2.7	15.4	35.7	4.1	9.1	7.6	99.8	423.8	18.4	83.9	8.5	1.3
n = 8	1σ	0.7	0.02	0.6	3.2	0.8	4.7	0.1	1.2	5.8	33.2	2.7	8.1	4.0	54.8	161.0	7.8	36.2	3.0	0.7
	1σ%	30%	32%	31%	24%	59%	8%	39%	43%	38%	93%	65%	88%	54%	55%	38%	42%	43%	35%	58%
	Maximum	3.8	0.09	2.7	18.4	3.0	68.2	0.7	5.4	22.9	112.8	9.6	28.4	14.7	229.5	741.3	31.0	132.7	14.0	2.3
	Minimum	1.1	0.00	1.2	8.6	0.3	53.3	0.2	1.6	2.9	12.2	1.7	3.0	2.3	48.0	106.3	4.6	7.5	3.7	0.4
	Median	2.5	0.06	1.5	13.2	1.1	61.3	0.3	2.4	15.2	20.1	3.3	6.3	7.1	86.7	417.4	18.4	87.7	7.9	1.1
5b-10.4b	Average	2.0	0.03	2.0	13.2	0.8	70.4	0.4	4.2	5.6	26.8	4.8	8.1	10.5	152.1	231.7	12.7	62.8	8.5	1.9
n = 9	1σ	0.6	0.02	0.3	2.4	0.2	3.7	0.1	1.2	1.5	9.8	1.4	2.2	4.0	49.7	74.7	8.3	52.2	2.8	0.8
	1σ%	28%	67%	16%	18%	28%	5%	27%	29%	26%	36%	29%	27%	38%	33%	32%	65%	83%	33%	43%
	Maximum	2.8	0.05	2.6	16.4	1.1	75.6	0.5	6.7	7.8	41.8	7.0	11.8	17.0	232.8	342.6	31.2	171.0	13.5	3.7
	Minimum	1.1	0.00	1.5	9.5	0.3	64.0	0.2	3.2	2.9	12.2	2.4	4.9	4.3	76.6	106.3	4.7	14.2	5.4	0.8
	Median	2.2	0.04	2.0	13.0	0.9	70.2	0.4	3.6	5.5	25.0	4.5	7.6	10.5	157.0	240.3	10.0	46.3	7.8	1.9
5d-1.72b	Average	3.3	0.05	1.8	14.2	1.2	65.8	0.5	2.9	8.7	33.6	5.3	10.2	10.5	79.5	246.6	17.6	86.2	11.9	1.3
n = 10	1σ	1.4	0.02	0.4	3.2	0.2	5.2	0.1	0.6	2.3	19.6	1.7	5.3	4.2	15.1	84.5	7.4	43.1	3.6	0.5
	1σ%	41%	31%	24%	23%	20%	8%	26%	20%	27%	58%	32%	52%	40%	19%	34%	42%	50%	30%	38%
	Maximum	6.9	0.08	2.6	22.8	1.6	73.6	0.7	3.4	14.7	81.0	9.6	22.4	20.6	94.8	408.7	35.7	151.3	19.0	2.3
	Minimum	2.1	0.02	1.2	11.1	0.8	53.3	0.3	1.6	5.8	17.6	3.3	5.1	5.8	48.0	153.0	9.9	37.6	7.9	0.8
	Median	3.0	0.06	1.7	13.3	1.2	66.8	0.5	3.1	8.3	25.9	5.1	9.6	9.5	83.6	210.1	14.6	88.8	10.6	1.1
Total analyses	Average	2.6	0.05	1.6	13.4	1.1	64.0	0.5	2.9	11.6	31.9	6.3	20.5	7.5	92.4	289.3	18.6	94.4	10.7	1.3
n = 119	1σ	1.0	0.03	0.6	3.0	0.3	6.1	0.2	1.4	7.4	20.5	3.2	33.7	3.9	51.4	140.7	9.4	158.1	5.2	0.8

Cs	Ba	La	Ce	Pr	Nd	Sm	Eu	Gd	Tb	Dy	Ho	Er	Tm	Yb	Lu	Hf	Ta	Pb	Th	U
2.3	767.6	24.7	43.6	5.5	21.7	4.1	0.9	3.8	0.6	3.7	0.8	2.5	0.4	3.0	0.5	17.5	0.9	74.0	17.3	6.3
1.2	156.9	4.7	8.4	1.0	4.0	0.8	0.1	0.7	0.1	0.9	0.3	1.1	0.2	2.1	0.4	37.5	0.2	112.1	23.8	3.8
51%	20%	19%	19%	18%	18%	19%	14%	19%	20%	25%	34%	46%	63%	70%	88%	214%	22%	152%	137%	60%
4.4	978.0	32.2	54.5	6.8	27.8	5.2	1.1	4.7	0.7	5.4	1.4	5.5	1.0	8.7	1.6	123.6	1.3	317.2	84.8	12.0
1.1	448.7	18.8	27.2	4.1	16.7	2.8	0.7	2.3	0.3	2.1	0.4	1.3	0.2	1.3	0.2	2.5	0.6	5.7	7.2	1.6
2.1	767.8	25.0	44.7	5.5	21.7	4.5	1.0	4.1	0.6	3.8	0.8	2.3	0.3	2.4	0.3	4.2	0.9	19.7	10.3	5.4
3.2	725.7	28.2	57.1	6.6	24.7	4.7	1.7	6.0	0.9	3.9	0.8	2.7	0.3	2.6	0.4	7.7	0.9	87.9	8.9	3.9
0.7	158.9	5.8	10.3	1.3	4.7	0.9	0.2	1.2	0.2	1.1	0.2	0.8	0.1	0.8	0.1	4.6	0.3	37.7	2.7	1.7
22%	22%	20%	18%	19%	19%	19%	13%	20%	21%	28%	27%	30%	35%	30%	35%	60%	33%	43%	30%	45%
4.6	1070.9	34.9	70.2	8.2	30.8	5.6	2.0	7.7	1.2	5.9	1.1	3.8	0.6	4.0	0.6	14.6	1.6	168.1	13.5	7.4
2.4	539.7	19.8	44.9	4.6	16.5	3.0	1.4	3.8	0.6	2.4	0.5	1.6	0.2	1.6	0.2	2.0	0.6	53.1	5.2	1.8
3.1	707.7	26.3	55.4	6.5	24.5	4.8	1.8	6.3	0.9	3.7	0.8	2.6	0.3	2.4	0.3	7.0	0.9	78.8	8.0	3.3
2.0	641.1	18.7	36.2	4.4	15.5	3.1	1.3	3.8	0.6	2.4	0.5	1.7	0.2	1.7	0.2	3.9	0.6	159.1	5.7	3.0
0.7	246.3	6.3	13.1	1.6	5.4	1.1	0.4	1.4	0.2	0.7	0.2	0.6	0.1	0.7	0.1	2.0	0.3	102.7	2.7	1.8
37%	38%	34%	36%	35%	35%	34%	34%	38%	32%	31%	37%	37%	37%	39%	43%	51%	47%	65%	48%	61%
3.4	1052.0	27.0	55.1	6.3	22.9	5.0	2.1	6.5	0.8	3.2	0.7	2.7	0.3	2.5	0.4	7.2	1.2	291.8	9.3	6.0
0.9	215.6	6.2	11.3	1.5	5.7	1.6	0.5	1.5	0.2	1.1	0.2	0.8	0.1	0.6	0.1	1.6	0.1	3.0	1.9	0.6
1.9	624.5	19.4	36.4	4.7	16.1	3.0	1.3	3.8	0.6	2.5	0.5	1.8	0.2	1.7	0.2	3.9	0.6	122.4	5.5	3.7
2.7	629.0	19.8	39.1	4.4	16.5	3.3	2.0	4.7	0.7	2.5	0.5	2.0	0.2	1.9	0.3	5.9	0.9	9.0	7.7	6.4
2.0	165.8	7.9	13.2	1.6	7.7	1.8	0.6	2.4	0.3	1.3	0.3	0.9	0.1	1.0	0.1	4.8	0.6	9.0	3.2	4.8
76%	26%	40%	34%	37%	47%	56%	30%	51%	47%	51%	51%	47%	43%	51%	46%	83%	68%	100%	41%	76%
7.1	850.1	33.2	58.4	6.6	27.8	5.8	3.0	8.7	1.3	4.4	0.9	3.4	0.4	3.5	0.5	14.9	2.1	29.6	13.4	15.8
0.6	437.3	9.9	19.6	2.2	6.2	0.7	1.2	1.3	0.2	0.7	0.2	0.7	0.1	0.6	0.1	1.2	0.2	2.3	3.3	0.9
2.2	620.4	18.6	40.9	4.4	14.9	2.9	1.9	4.0	0.6	2.4	0.5	1.8	0.2	1.8	0.3	4.4	0.7	6.4	7.3	4.5
4.0	834.3	24.5	57.0	5.9	20.7	3.6	0.9	2.9	0.4	2.7	0.5	1.7	0.3	2.2	0.3	7.6	1.0	10.5	8.7	5.1
2.7	173.9	16.3	40.0	3.6	11.3	1.5	0.2	1.0	0.1	0.9	0.2	0.6	0.1	1.0	0.2	6.0	0.8	7.8	4.3	2.9
68%	21%	67%	70%	61%	54%	41%	19%	36%	33%	33%	32%	37%	38%	47%	52%	79%	83%	75%	49%	57%
11.1	1182.1	67.5	164.8	15.1	48.3	6.3	1.1	4.5	0.6	4.0	0.8	2.5	0.4	4.0	0.7	18.2	3.2	26.4	17.8	9.5
1.5	666.2	4.5	13.0	1.1	3.6	0.6	0.5	0.5	0.1	0.5	0.2	0.3	0.1	0.6	0.1	2.3	0.2	1.3	1.9	1.7
3.7	770.4	20.1	49.4	5.3	19.4	3.7	1.0	3.1	0.4	2.9	0.6	1.7	0.2	1.9	0.3	4.6	0.8	9.3	7.9	4.4
2.2	642.3	26.1	49.2	6.1	23.3	4.3	1.4	5.4	0.7	3.1	0.6	2.2	0.3	2.1	0.3	5.6	0.7	29.9	8.4	4.3
1.1	182.4	11.8	22.5	2.9	10.7	1.9	0.5	2.3	0.3	1.1	0.2	0.8	0.1	0.7	0.1	2.6	0.3	33.2	3.3	3.8
48%	28%	45%	46%	48%	46%	45%	37%	43%	44%	36%	34%	35%	34%	36%	36%	46%	38%	111%	39%	89%
3.8	835.8	45.5	84.2	11.7	43.4	8.1	2.4	9.9	1.4	5.1	0.9	3.4	0.4	3.0	0.5	9.1	0.9	116.2	11.7	15.4
0.6	223.6	7.8	13.4	2.0	7.2	1.4	0.5	2.0	0.3	1.2	0.2	0.8	0.1	0.7	0.1	0.9	0.2	6.9	2.0	2.2
2.7	682.0	24.9	47.4	5.6	22.0	4.1	1.5	5.0	0.7	3.3	0.6	2.3	0.3	2.2	0.3	5.7	0.8	13.9	8.9	3.0
3.4	777.5	34.1	56.9	7.9	30.7	5.9	1.6	7.4	1.1	4.8	1.0	3.2	0.4	2.9	0.4	6.3	0.9	10.2	58.3	3.8
0.9	229.9	34.6	32.2	8.1	33.0	6.3	0.5	7.6	1.0	3.5	0.6	1.9	0.2	1.1	0.2	4.4	0.3	6.1	137.9	2.0
27%	30%	101%	57%	103%	108%	107%	30%	103%	96%	73%	60%	58%	42%	38%	40%	70%	32%	60%	236%	51%
4.8	1368.0	131.4	145.1	30.9	123.6	23.7	2.7	28.7	4.0	13.9	2.3	7.9	0.8	4.9	0.7	18.2	1.6	25.7	448.2	8.6
1.6	608.6	18.3	39.5	4.2	14.9	3.1	1.1	3.3	0.5	2.4	0.5	1.7	0.2	1.4	0.2	2.5	0.5	3.0	6.0	2.0
3.1	683.7	22.2	44.3	5.0	18.9	3.6	1.4	4.9	0.7	3.7	0.8	2.8	0.4	2.9	0.4	5.1	0.9	9.3	9.4	3.3
2.5	759.1	23.3	40.9	5.4	19.8	3.6	0.8	2.9	0.4	2.7	0.5	1.6	0.2	1.9	0.3	4.3	1.0	809.8	9.6	5.9
1.2	309.6	12.4	15.0	3.5	11.8	2.3	0.4	1.6	0.2	1.5	0.3	0.9	0.1	1.2	0.2	3.9	0.8	517.7	12.7	10.1
47%	41%	53%	37%	65%	60%	62%	43%	53%	54%	58%	58%	57%	64%	63%	66%	90%	84%	64%	133%	173%
5.0	1692.3	60.9	69.6	17.4	56.5	10.3	1.6	6.5	1.0	6.9	1.4	4.3	0.7	5.4	0.7	14.6	3.8	1734.7	57.0	44.8
0.8	387.2	12.9	25.8	2.9	10.4	1.9	0.5	1.5	0.2	1.4	0.3	0.8	0.1	1.0	0.1	1.0	0.4	50.1	0.7	1.5
2.7	759.6	17.8	33.7	4.1	14.5	2.8	0.6	2.3	0.4	2.0	0.4	1.2	0.2	1.4	0.2	2.9	0.6	829.5	6.1	3.4
1.3	960.9	26.8	43.1	5.6	22.8	4.4	0.9	4.0	0.6	4.2	1.0	2.7	0.4	3.0	0.5	7.0	0.9	3.3	12.5	8.8
0.6	237.9	6.6	12.0	1.5	6.0	1.2	0.2	1.2	0.2	1.4	0.3	1.0	0.2	1.2	0.2	2.3	0.2	1.7	4.5	2.5
49%	25%	25%	28%	26%	26%	27%	24%	31%	32%	33%	36%	38%	38%	39%	41%	34%	25%	51%	36%	28%
2.7	1212.8	34.7	57.0	7.6	31.0	6.1	1.2	5.9	1.0	6.2	1.4	4.4	0.7	4.9	0.8	10.8	1.2	6.8	23.6	12.9
0.8	479.0	13.3	19.8	2.8	11.1	2.2	0.5	2.0	0.3	2.0	0.4	1.2	0.2	1.1	0.2	3.1	0.5	1.1	5.6	4.1
1.1	1031.8	28.7	47.7	5.8	24.6	4.5	1.0	3.9	0.7	4.5	1.0	2.6	0.4	3.0	0.5	6.7	1.0	2.8	11.4	8.8
2.7	818.5	24.0	40.3	5.2	21.4	3.9	0.9	3.6	0.5	3.4	0.6	1.8	0.3	2.0	0.3	4.3	0.8	10.4	18.1	6.4
1.4	455.3	9.2	16.0	2.0	8.7	1.6	0.4	1.5	0.3	1.4	0.3	0.7	0.1	0.9	0.2	1.9	0.3	6.6	20.1	5.1
53%	56%	38%	40%	38%	41%	41%	46%	42%	48%	43%	45%	40%	46%	43%	53%	45%	32%	64%	111%	80%
6.0	1797.2	38.7	69.1	8.3	35.0	6.0	1.4	5.6	0.9	5.8	1.2	2.9	0.5	3.4	0.6	7.0	1.3	24.8	66.5	15.4
1.2	122.8	8.3	13.6	1.8	6.9	1.2	0.3	1.0	0.1	0.8	0.2	0.5	0.1	0.5	0.1	0.4	0.3	3.9	1.6	0.3
2.2	705.7	23.5	40.7	5.0	20.9	3.9	0.8	3.5	0.5	3.2	0.7	1.9	0.3	2.1	0.3	4.5	0.8	9.2	12.9	5.0
4.6	700.1	18.9	41.8	4.4	15.8	2.8	0.8	2.4	0.4	2.2	0.4	1.4	0.2	1.6	0.2	3.3	0.7	12.2	7.2	2.4
2.0	303.0	8.3	16.4	1.8	6.7	1.2	0.3	1.1	0.2	1.3	0.3	0.9	0.2	1.2	0.2	2.5	0.3	5.6	3.0	1.6
43%	43%	44%	39%	41%	42%	44%	30%	47%	51%	58%	64%	67%	74%	74%	70%	78%	51%	46%	42%	66%
8.3	1071.5	31.1	69.7	7.5	27.4	5.1	1.2	4.4	0.8	4.9	1.1	3.3	0.6	4.4	0.6	8.9	1.3	24.7	11.2	5.4
2.2	122.8	9.7	23.4	2.4	8.4	1.4	0.4	1.2	0.2	0.8	0.2	0.5	0.1	0.5	0.1	0.9	0.3	7.4	3.9	0.9
4.8	660.6	16.7	36.0	3.7	13.8	2.4	0.9	2.1	0.3	1.8	0.4	1.0	0.2	1.2	0.2	2.6	0.5	11.6	6.5	1.7
2.6	665.1	36.4	78.4	8.7	31.9	5.8	1.0	4.4	0.6	3.1	0.6	1.8	0.3	2.2	0.3	5.0	0.8	9.5	21.4	3.3
0.7	201.7	46.8	100.1	10.7	38.1	6.6	0.3	4.1	0.4	1.1	0.2	0.7	0.1	0.9	0.1	2.5	0.4	5.4	43.1	1.6
26%	30%	129%	128%	122%	119%	113%	33%	93%	63%	37%	38%	37%	45%	43%	45%	51%	44%	57%	201%	49%
3.2	997.3	168.3	362.1	39.0	139.7	24.6	1.9	15.8	1.6	5.4	1.1	3.3	0.6	4.2	0.6	9.5	1.8	17.2	144.0	5.8
1.2	297.2	12.6	31.3	3.5	13.2	2.5	0.8	2.3	0.3	1.9	0.3	1.0	0.2	1.1	0.1	2.3	0.5	3.9	5.0	1.2
2.7	712.1	23.7	48.5	5.4	20.0	3.9	1.0	3.3	0.5	2.7	0.5	1.6	0.2	1.9	0.3	5.0	0.7	8.2	8.1	2.9
2.7	747.5	25.5	48.5	5.9	22.1	4.1	1.2	4.2	0.6	3.2	0.6	2.1	0.3	2.2	0.3	6.5	0.9	145.2	15.2	5.1
1.6	256.1	18.9	35.1	4.4	16.5	3.0	0.5	3.0	0.4	1.7	0.3	1.1	0.2	1.2	0.2	11.4	0.5	335.0	43.0	4.9

(continued on next page)

Table 4 (*continued*)

Sample number		FeO	MnO	Na_2O	Al_2O_3	MgO	SiO_2	TiO_2	K_2O	CaO	Cr[a]	Co	Cu	Ga	Rb	Sr	Y	Zr	Nb	Sn
Total Analyses n=19	1σ%	36%	53%	34%	22%	32%	9%	40%	47%	64%	64%	50%	164%	52%	56%	49%	50%	167%	49%	64%
	Maximum	7.5	0.18	3.2	22.8	3.0	75.6	1.6	10.4	38.4	136.4	17.0	312.3	20.6	327.9	752.8	61.8	1682.2	41.7	6.8
	Minimum	0.7	0.00	0.4	3.8	0.2	47.5	0.0	0.7	1.3	6.4	1.1	2.6	1.7	20.3	18.6	3.7	6.2	0.4	0.4
	Median	2.5	0.05	1.6	13.5	1.1	65.1	0.4	2.8	8.8	26.9	5.9	10.3	6.8	85.6	242.1	17.4	62.7	10.4	1.1

Major elements are reported in wt.%.
[a] Trace elements are reported in μg/g.

investigated here can be attributed to mixing between phases naturally present within the sand. The patterns displayed in Fig. 5 indicate that most of the trace elements contain concentrations similar to those of the un-melted sand. Outliers have been categorized and grouped based on minerals typically found in arkosic sand.

Trace element patterns shown in Fig. 5 have depletions in metals (i.e., Cr and Co). Copper, Pb, Th, and U record the largest variations in elemental concentrations, with each spanning several orders of magnitude. The enriched metals (Cu and Pb) show no systematic trends in enrichment or depletion and are not considered in the following discussion. There are no systematic trends from left to right in Fig. 5 for individual trinitite analyses, suggesting the lack of temperature-controlled elemental fractionations, which would result in a negative slope. Samples shown in Fig. 5A display the flattest patterns and therefore these are considered to represent "non-mineral enriched" trinitite compositions. Hence, these analyses likely represent the best-homogenized trinitite source material. Fig. 5B illustrates analyses that are similar to "non-enriched" trinitite (Fig. 5A), except for the relative enrichment in U without any other systematic elemental enrichments; the origin of U will be discussed below.

Fig. 5C–E shows patterns with certain trace element enrichments attributable to accessory minerals (i.e., ilmenite, zircon, monazite, apatite) common in arkosic sand. For example, the presence of ilmenite (Fig. 5C) is diagnosed by correlated enrichments in Nb, Ta and TiO_2 contents (Fig. 4) relative to the remaining elements. Of interest, the two analyses of trinitite that contain exceptionally large enrichments in Nb and Ta also have trace element concentrations similar to the other trinitite samples. This similarity in trace element abundances further suggests an anthropogenic source for Nb and Ta for these two analyses. The presence of zircon (Fig. 5D) is identified by the parallel enrichments in Zr, Hf, U, Y, and heavy rare earth elements (HREEs). The incorporation of monazite and/or apatite (Fig. 5E) is identified by enrichments in Th, Y, and light rare earth elements (LREEs). An overall, general depletion in Zr is observed and is due to the different sample processing methods; i.e., whole rock dissolution (un-melted sand) vs. spatially resolved spot analysis by LA–ICP-MS (trinitite glass). Zircon is present at low modal abundance within arkosic sand and consequently it is difficult to detect Zr-rich melt glass on a consistent basis via laser ablation analysis.

5.3.2. Origin of trace elements

While trace element patterns display vital information for fingerprinting geochemical characteristics, PCA (e.g., Fig. 6) can be used to further investigate and better elucidate the behavior of major and trace elements. PCA is a type of multivariate analysis that is best used on large datasets, such as the one presented here. The PCA were conducted on each compositional grouping of trinitite, based on trace element patterns (e.g., non-enriched and U-enriched), using MATLAB software by MathWorks (Fig. 6). PCA ultimately results in a way to visualize, in a single diagram, the variable chemical composition of each trinitite group for the elements investigated here. To perform PCA, the original datasets must be converted into a matrix that is pairwise correlated between the variables, which in this case are the chemical compositions. The correlated tables along with the original data are reported in the Supplementary materials. Once the matrices are correlated, the principal components are calculated by using the inverse variances of the chemical compositions as weights. This "weighted" approach allows for direct comparison of variability in chemical composition between different units of measurement (i.e., wt.% vs. μg/g). After the principal components are calculated, the first three principal component coefficient vectors are calculated. Using the weights as a scalar, the matrix can then be converted into equivalent orthogonal coefficients. Once the new matrix is orthogonal, the data can be plotted on a new coordinate system defined by the principal components. After re-plotting the data on principal component axes (red symbols in Fig. 6), the variability in each chemical species can be plotted as a vector. This vector describes the chemical behavior of each element and is displayed in Fig. 6. The direction and length of the vector indicate how each chemical species behaves in relation to the two principal components. The PCA are used here to constrain the phases controlling the major and trace element abundances and to corroborate observations made in the trace element patterns and major/trace element diagrams (Figs. 3, 4, 5).

Fig. 6A illustrates the PCA for the non-enriched trinitite. K_2O, Al_2O_3, Na_2O, Pb, Rb, Cs, and SiO_2 all share relatively the same direction indicative of a strong K-feldspar component. Barium and Ga are distinct from all other species. The presence of Ba is likely due to barite in the sand. The unique behavior of Ga may be attributed to its addition from the device's core since it was alloyed with the Pu. Strontium, MgO, and CaO share similar directions and are likely due to the presence of various carbonates (i.e., calcite, dolomite). Iron oxide, Co, TiO_2, and MnO are all likely derived from the tower, ilmenite, and/or magnetite. Uranium, Nb, Ta, Th, Cu, Cr, Hf, and the REEs all have roughly the same direction indicating similar behavior. Therefore, the abundances of the REEs, Zr, Th, and by geochemical association Y and Hf (Bea, 1996) in trinitite are likely controlled by the presence of U-bearing trace phases (zircon, monazite, and/or apatite). Interestingly, Ta and Nb behave differently relative to Ti, further suggesting derivation from an anthropogenic source. The vectors for U and Cu have a similar direction suggesting that some of the U in these analyses is anthropogenic.

Fig. 6B represents the vector analysis of the U-enriched trinitite. Once again, as in Fig. 6A, there are similar K-feldspar and calcite/limestone components. Titanium, Nb, and Ta all behave similarly and may be related to the presence of ilmenite. The REE elements share the same direction along with Hf and Th, which indicate derivation from a natural source. Uranium behaves similarly to Cu, Cr, FeO, Co, and MgO, but distinctly from Hf, which suggests the U in these analyses is a mix between natural and anthropogenic components.

Fig. 6C documents the Nb- and Ta-enriched trinitite. Niobium and Ta behave similarly but are extremely different relative to Ti. The K-feldspar component is indicated by the similarity in K_2O, Cs, and Rb vectors. Thorium behaves differently than the REEs, which indicates the majority of latter originate from U-bearing minerals. Chromium, Co, MnO, and MgO all behave similarly, and Pb and Cu behave almost identically. The increased spread in vector directions for all of the other elements is likely a result of the small number of data for this analysis ($n = 6$) compared to the previous analysis ($n \sim 40$).

Fig. 6D represents the PCA for the Zr-enriched trinitite. The SiO_2, K_2O, Na_2O, Cs, Rb, and Eu vectors illustrate the K-feldspar component. The light REEs behave similarly to Th, whereas vectors for the heavy REEs are similar to those for U, Zr, and Hf. This discrepancy indicates an origin for the LREEs in a Th bearing mineral (monazite, apatite) and the HREEs in zircon. Strontium and CaO behave nearly identically, indicating

Cs	Ba	La	Ce	Pr	Nd	Sm	Eu	Gd	Tb	Dy	Ho	Er	Tm	Yb	Lu	Hf	Ta	Pb	Th	U
57%	34%	74%	72%	75%	74%	73%	44%	72%	66%	52%	51%	52%	53%	53%	61%	176%	55%	231%	282%	97%
11.1	1797.2	168.3	362.1	39.0	139.7	24.6	3.0	28.7	4.0	13.9	2.3	7.9	1.0	8.7	1.6	123.6	3.8	1734.7	448.2	44.8
0.6	122.8	4.5	11.3	1.1	3.6	0.6	0.3	0.5	0.1	0.5	0.2	0.3	0.1	0.5	0.1	0.4	0.1	1.1	0.7	0.3
2.7	731.4	22.9	44.9	5.2	20.0	3.7	1.0	3.8	0.6	3.0	0.6	2.0	0.3	2.1	0.3	4.7	0.8	12.5	8.2	3.7

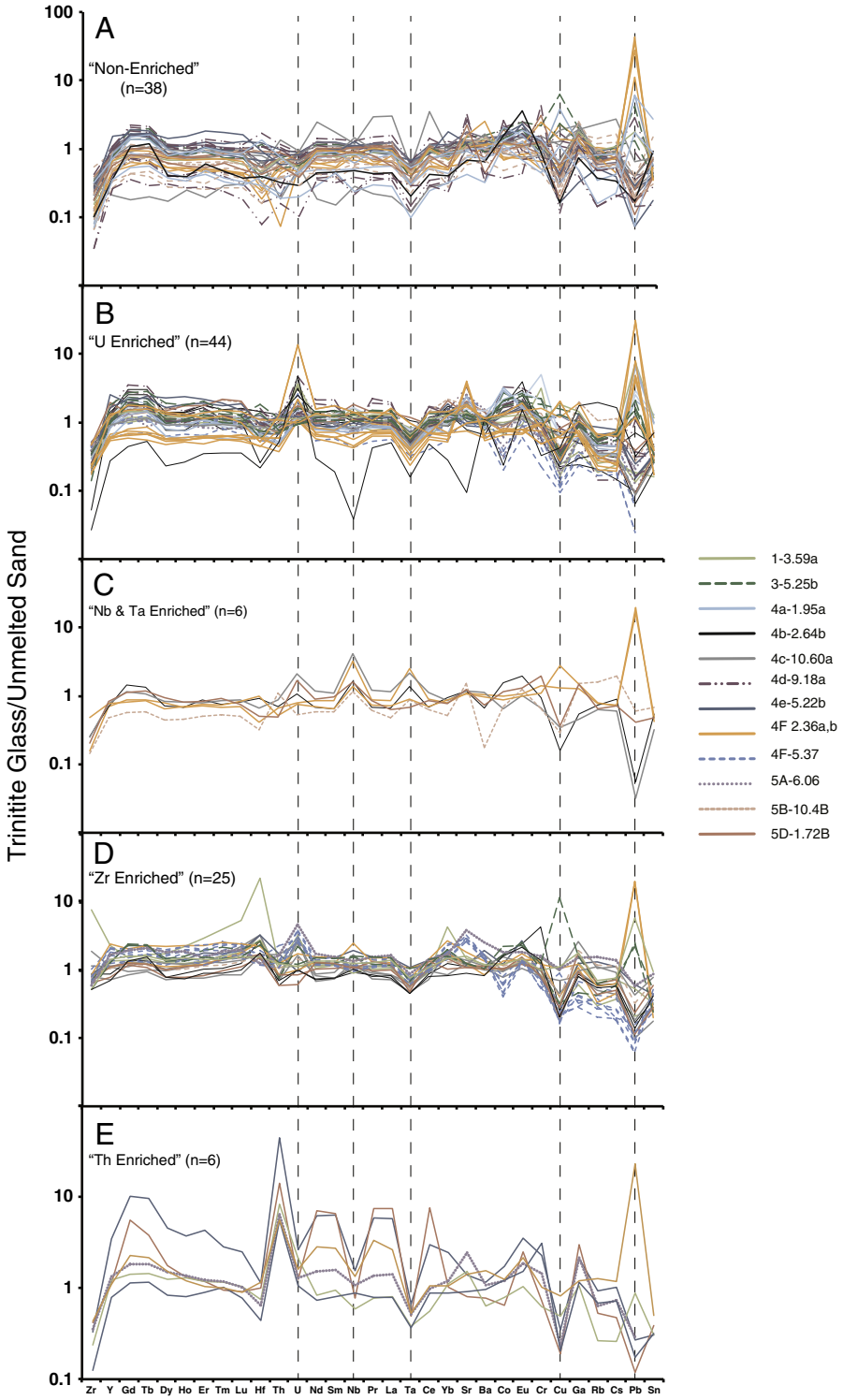

Fig. 5. Normalized trace element diagrams. Elements ordered by decreasing condensation temperatures (Lodders, 2003) and normalized to concentrations of loose sand present on the bottom side of trinitite samples.

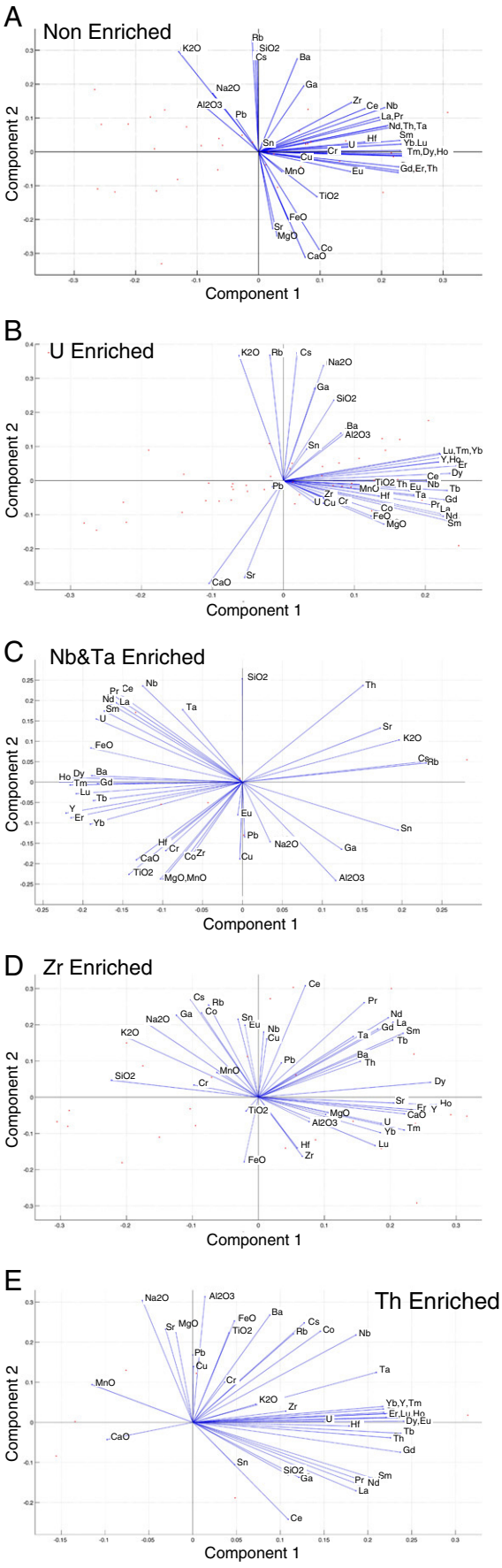

the presence of carbonate. Iron behaves distinctly and suggests the presence of magnetite. Copper and Pb display similar vectors, as is the case for Cr, Co, and MnO but these define different vectors compared to other metals.

Fig. 6E illustrates the PCA of the Th-enriched trinitite and similar trends are present here as in the other PCA (Fig. 6A–D). Lead, Cu, MgO, and Al_2O_3 vectors display similar behaviors. Iron oxide and TiO_2 are identical, while different from Nb and Ta. Both K-feldspar and calcite components are present as defined in Fig. 6A–D. Lastly, as with the previous PCA diagrams, a U/Th-bearing mineral seems to be controlling the distribution of the REEs.

Overall, the PCA corroborates the interpretations based on the trends defined by the major and trace element data (Figs. 3, 4, and 5), and the chemical composition of trinitite blast melt consists of a mixture of certain precursor minerals and an anthropogenic component. The natural precursor minerals are K-feldspar, calcite, quartz, barite, ilmenite, and U/Th-bearing minerals such as monazite, apatite, and zircon. Gallium seems to have a distinct behavior in all of the PCA, possibly indicating an anthropogenic/gadget source. The metals (Co, Cr, Cu, Pb) reported in this study are not expected to be present in the precursor arkosic sand at the abundances measured here. Reasonably similar vector directions are seen in most of the PCA for Co, Cr, Cu, and Pb (Fig. 6). Chromium and Co are trace elements present in steel and could represent input from the blast tower, whereas Cu was present as wiring used in Gadget and monitoring equipment. The similarity in behavior between these metals indicates mixing between the same two end-members, namely anthropogenic (Gadget and blast tower) and the arkosic sand. Inclusions of CuS and PbO have been observed on the surface of trinitite glass and were attributed to melted wiring and possibly the tamper or other materials at the blast site (Bellucci and Simonetti, 2012). Such inclusions may also have been melted/incorporated within the trinitite glass. The behavior of U is not always correlated with Zr, Th, and the REEs indicating at least two likely sources: 1) indigenous U from zircon, monazite and/or apatite and 2) the tamper used in the Gadget.

5.4. Temperature effects

The concentrations of the volatile anthropogenic metals (Co, Cr, Cu, and Pb) are enriched in samples that originate from >74 m away (no ^{152}Eu activity, Bellucci et al., 2013a) from ground zero compared to samples closer to ground zero (51–74 m; Table 5, Fig. 7). Table 5 lists the average concentrations for all analyses for samples that originate 51–74 m from ground zero (n = 74), samples that originate >74 m from ground zero (n = 43), condensation temperature (50% T_C (K) from Lodders, 2003), and % enrichment (((concentration < 74 m) −(concentration - 74 m) / (concentration < 74 m)) * 100) between the two distance ranges. The metals shown in Fig. 7 have relatively low condensation temperatures and would condense from a gas phase into a liquid or solid with decreasing temperature. Therefore, volatile metals are preferentially concentrated on the periphery of the blast site where the temperature is depressed compared to that at ground zero. Additionally, the % enrichment of these metals for samples that originate >74 m away from ground zero correlate with their respective condensation temperatures (Fig. 7). Thus, the increase in the concentrations of anthropogenic-related volatile metals (e.g., Pb, Cu) towards the edge of the blast zone suggests that the peripheral areas may be critical areas for identifying nuclear metal components during forensic analysis of post-detonation materials.

Fig. 6. Principal component analysis for each trinitite group (as defined by trace element data—Fig. 5). Pink dots represent the re-calculated data plotted against the principal components.

Table 5
Average concentration of volatile metals, condensation temperature, and % increase after 74 m.

Condensation temperature		Average concentration		Average concentration		
50% T_C (K)[a]	Element	<74 m	$1\sigma_{mean}$ (n = 74)	>74 m	$1\sigma_{mean}$ (n = 43)	% increase
1352	Co	5.9	0.3	7.2	0.5	22%
1296	Cr	29.5	0.2	35	3	19%
1037	Cu	12	1	35	8	192%
727	Pb	12	2	355	69	2858%

[a] From Lodders (2003).

6. Conclusions

The chemical compositions of trinitite glass at high spatial resolution reported here are largely dependent on the phases present during melting. Major element contents of trinitite indicate mixing between major minerals typically found in arkosic sand including: quartz, K-feldspar, and calcite or gypsum. In addition to natural minerals, an anthropogenic component is implied by enrichments in the contents of Al_2O_3, FeO, MgO and MnO, which are not possible given the available mineral assemblage typical of arkosic sand. Trace element compositions of trinitite indicate mixing between major and minor phases present in arkosic sand including: calcite or gypsum (Sr), barite (Ba), K-feldspar (Rb, Cs), ilmenite (Nb, Ta), monazite or apatite (Y, Th, REE), and zircon (Zr, Y, Th, Hf, REE). The concentrations of metals (Co, Cr, Cu, Pb, and some Nb and Ta) are highly variable and their presence can be largely attributed to the incorporation of components from the Gadget and/or blast tower. Gallium displays a unique chemical behavior and could be from the core of the device. Uranium in trinitite most likely originates from two distinct sources: U-bearing phases (zircon, monazite, and apatite) and the natural U-tamper.

The abundances of Co, Cu, Cr, and Pb are higher in samples that originate >74 m away from ground zero and the degree of enrichment is dependent on their respective condensation temperatures. The enrichment of volatile metals towards the periphery of the blast site indicates that this region is optimal for their sampling in relation to forensic investigations.

Acknowledgments

The authors thank Dr. Ian Steele for his expertise with electron microprobe analysis. Sandy Dillard of the Brazos Valley Petrographic Thin Section Services Lab (Bryan, Texas) is thanked for the production of high quality thin sections of trinitite. Drs. Nelson Eby, Jerome Sterpenich, Chief Editor Laurie Reisberg, and an anonymous reviewer are thanked for constructive comments on an earlier draft of this manuscript. This research work was funded by DOE/NNSA grant PDP11-40/DE-NA0001112.

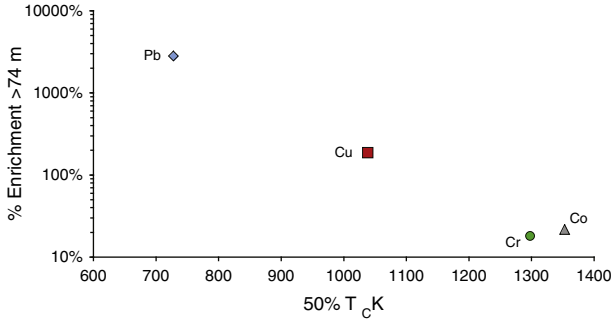

Fig. 7. Enrichment of volatile metals (%) between samples that originate close to ground zero (51–74 m) and those further (>74 m) away vs. condensation temperature (50% T_C (K)).

Appendix A. Supplementary data

Supplementary data to this article can be found online at http://dx.doi.org/10.1016/j.chemgeo.2013.12.001.

References

Bea, F., 1996. Residence of REE, Y, Th, and U in granites and crustal protoliths; implications for the chemistry of crustal melts. J. Petrol. 37 (3), 521–552.
Bellucci, J.J., Wallace, C., Koeman, E., Simonetti, A., Burns, P., Kieser, J., Port, E., Walczak, E., 2013a. Distribution and behavior of some radionuclides in the Trinity nuclear test. J. Radioanal. Nucl. Chem. 295 (3), 2049–2057.
Bellucci, J.J., Simonetti, A., Wallace, C., Koeman, E.C., Burns, P., 2013b. Isotopic fingerprinting of the world's first atomic device. Anal. Chem. 85, 4195–4198. http://dx.doi.org/10.1021/ac400577p.
Bellucci, J.J., Simonetti, A., Wallace, C., Koeman, E.C., Burns, P., 2013c. The Pb isotopic composition of trinitite melt glass: evidence for the presence of Canadian industrial Pb in the first atomic weapon test. Anal. Chem. 85, 7588–7593. http://dx.doi.org/10.1021/ac4016648.
Bellucci, J.J., Simonetti, A., 2012. Nuclear forensics: searching for nuclear device debris in trinitite-hosted inclusions. J. Radioanal. Nucl. Chem. 293, 313–319.
Belloni, F., Himbert, J., Marzocchi, O., Romanello, V., 2011. Investigating incorporation and distribution of radionuclides in trinitite. J. Environ. Radioact. 102, 852–862.
Chen, W., Simonetti, A., 2013. In-situ determination of major and trace elements in calcite and apatite, and U–Pb ages of apatite from the Oka carbonatite complex: insights into a complex crystallization history. Chem. Geol. 353, 151–172.
Eby, N., Hermes, R., Charnley, N., Smoliga, J.A., 2010. Trinitite—the atomic rock. Geol. Today 26 (5), 180–185.
Fahey, A.J., Zeissler, C.J., Newbury, D.E., Davis, J., Lindstrom, R.M., 2010. Postdetonation nuclear debris for attribution. Proc. Natl. Acad. Sci. 107 (47), 20207–20212.
Hainley, T.J., Smierciak, M.F., Welsh, N.P., Simonetti, A., Bellucci, J.J., Koeman, E.C., Wallace, C., 2012. A compositional investigation of postdetonation nuclear debris: results from in situ investigations of trinitite glass (poster presentation). 2012 Geological Society America Annual Meeting, Charlotte NC, Nov. 4–7, 2012.
Jenner, G.A., Longerich, H.P., Jackson, S.E., Freyer, B.J., 1990. ICP-MS—a powerful tool for high precision trace element analyses in earth sciences: evidence from analyses of selected U.S.G.S. reference samples. Chemical Geology 83, 133–148.
Koeman, E.C., Wallace, C.M., Simonetti, A., 2012. 3-Dimensional distribution of chemical constituents of trinitite. MARC IX: Ninth International Conference on Methods and Applications of Radioanalytical Chemistry, Kailua-Kona, Hawaii, March 25–30, p. 2012.
Lodders, K., 2003. Solar system abundances and condensation temperatures of the elements. Astrophys. J. 591, 1220–1247.
Love, D.W., Allen, B.D., Myers, R.G., 2008. Gypsum crystal morphologies and diverse accumulations of gypsum and other evaporites in the Tularosa basin. N. M. Geol. 30, 120–121.
Parekh, P.P., Semkow, T.M., Torres, M.A., Haines, D.K., Cooper, J.M., Rosenburg, P.M., Kitto, M.E., 2006. Radioactivity in trinitite six decades later. J. Environ. Radioact. 85, 103–120.
Pettijohn, F.J., 1963. Chapter S: the chemical composition of sandstones—excluding carbonate and volcanic sands. In: Fleischer, M. (Ed.), Data of Geochemistry. U.S. Geological Survey Professional Paper, 440-s (19 pp.).
Ross, C.S., 1948. Optical properties of glass from Alamogordo, New Mexico. Am. Mineral. 33, 360–362.
Rhodes, R., 1986. The Making of the Atomic Bomb, 1st ed. Simon and Schuster, New York 575–577 (657).
Rudnick, R.L., Gao, S., 2003. The composition of the continental crust. In: Rudnick, R.L. (Ed.), The Crust. In: Holand, H.D., Turekian, K.K. (Eds.), Treatise on Geochemistry, vol. 3. Elsevier-Pergamon, Oxford, pp. 1–64.
Schlauf, D., Siemon, K., Weber, R., Esterlund, R.A., Molzahn, D., Parzelt, P., 1997. Trinitite redux: comment of "Determining the yield of the Trinity nuclear device via gamma-ray spectroscopy" by David Arkatz and Christopher Bragg. Am. J. Phys. 63, 411–413.
Semkow, Thomas M., Parekh, Pravin P., Haines, Douglas K., 2006. Modeling the effects of the Trinity test. Appl. Model. Comput. Nucl. Sci. 142–159.
Staritzky, E., 1950. Thermal Effects of Atomic Bomb Explosions on Soils at Trinity and Eniwetok. Los Alamos Scientific Laboratory 21 (LA-1126).
Storms, B., 1965. Trinity. Atom 2 (8), 1–34.

US GPO, 2000. Trinity Site July 16, 1945. US Government Printing Office: 2000-844-916, Washington, DC.

van Achterbergh, E., Ryan, C.G., Jackson, S.E., Griffin, W., 2001. Data reduction software for LA–ICP-MS. Laser ablation–ICPMS in the earth sciences. Mineralogical Association of Canada Short Course, 29, pp. 239–243.

Wallace, C., Bellucci, J.J., Simonetti, A., Koeman, C., Hainley, T., Burns, P.C., 2013. A multi-method approach for determination of radionuclide distribution in trinitite: implications for explosion debris formation. J. Radioanal. Nucl. Chem. 298, 993–1003. http://dx.doi.org/10.1007/s10967-013-2496-8.